

Uncovering Planetary Nebulae in Early Type Galaxies using the Rutgers Fabry-Perot

Arend P. N. Sluis^{1,2} and T.B. Williams¹

*Department of Physics & Astronomy, Rutgers University,
136 Frelinghuysen Road, Piscataway, NJ 08854*

sluis@physics.rutgers.edu, williams@physics.rutgers.edu

ABSTRACT

We report on observations of four early-type galaxies performed with the Rutgers Fabry-Perot in order to search for Planetary Nebulae (PNe) in these systems. The aim is to use the PNe as kinematic tracers of the galaxy potential. We describe our data reduction and analysis procedure and show that the proper calibration of our detection statistic is crucial in getting down to our limiting magnitude of $m_{5007} = 26.1$. In the case of the two Leo galaxies we find moderately sized samples: 54 PNe in NGC 3379 and 50 PNe in NGC 3384; NGC 4636 (2 PNe) and NGC 1549 (6 PNe) are included for completeness. We present our samples in tabular form, as well as the spectrum for each PN. We constructed simple non-parametric spherical mass models for NGC 3379 using a Monte Carlo Markov Chain method to explore the space of likely mass models. We find a remarkably constant mass-to-light ratio within five half-light radii with an overall B band mass-to-light ratio ~ 5 . A simple mass-to-light estimate for NGC 3384 yields $\Upsilon_B \sim 11$, but is likely an overestimate.

Subject headings: instrumentation: spectrographs — galaxies: elliptical and lenticular, cD — galaxies: kinematics and dynamics — planetary nebulae: general

1. Introduction

The existence of Dark Matter (DM) has been postulated to resolve the conflict between dynamical estimates of galaxy and galaxy cluster masses, and estimates of their luminous or baryon mass. DM, as a source of gravitational potential, is an essential ingredient in the current Λ CDM

¹Visiting Astronomer, Cerro Tololo Inter-American Observatory. CTIO is operated by AURA, Inc. under contract to the National Science Foundation.

²Current address: Dept. of Astronomy, University of Massachusetts, LGRT-B 619E, 710 N. Pleasant St., Amherst, MA 01003; email: sluis@astro.umass.edu.

concordance cosmology of the Universe as derived from observations of the Cosmic Microwave Background (Spergel et al. 2003) and high redshift Supernova searches (Riess et al. 1998; Perlmutter et al. 1999). Little consensus exists, however, on its properties at smaller galactic scales with observations (e.g. de Blok et al. 2003) and numerical simulations (e.g., Diemand et al. 2004) currently being at odds. Indeed, the lack of a consistent understanding of DM has led some to question the necessity of the DM postulate (Sellwood & Kosowsky 2001).

An important diagnostic in the study of DM is its distribution throughout a galaxy. The strongest constraints come from observations of spiral galaxies, where neutral hydrogen gas can be used to detect the influence of DM beyond the stellar disk (Sofue & Rubin 2001). The case for DM in the more massive elliptical galaxies is less concrete. Unlike the simpler geometry of disk galaxies, the intrinsic three-dimensional shape of an elliptical cannot be uniquely determined from its projected shape. Similarly, the orbital structure of ellipticals is dominated by random motion, whereas the stars and gas in spiral galaxies move on nearly circular orbits. These fundamental limitations are exacerbated by practical ones. Because the galaxy surface brightness drops steeply as a function of radius, measurements of the stellar kinematics in ellipticals do not extend far into the galaxy halo, and require substantial observational effort. Furthermore, their gas content is low, and surveys of tracer populations such as globular clusters and planetary nebulae have until recently generated only modestly sized samples, the one exception being Cen A (Hui et al. 1995). The picture is only discouraging in contrast to the observations of disk galaxies, however, and—taken in their own right—the recent data on elliptical galaxies have greatly improved the understanding of these systems.

Measurements of the stellar kinematics in ellipticals now include higher order moments of the line-of-sight velocity distribution (LOSVD) as a matter of course (e.g., Carollo et al. 1995). Knowledge of the actual LOSVD, as opposed to only the first and second moments, can lift the degeneracy between the mass distribution and the velocity structure (Gerhard 1993; Merritt 1993). Along with more sophisticated modeling techniques, the observations, sometimes going out as far as two effective (half-light) radii (R_e), have allowed for a better constrained dynamical picture of a growing number of ellipticals (for references, see Kronawitter et al. 2000). Most intriguingly, the circular velocity curves in the Kronawitter et al. (2000) sample are quite flat, indicative of the presence of a DM halo. Despite this, no clear trends have emerged about the DM distribution in ellipticals, with some galaxies showing evidence for DM within $2R_e$ (mass-to-light ratio in the B band $\Upsilon_B \sim 20\text{-}30$), and others showing little or no evidence (Kronawitter et al. 2000).

Gas is scarce in early-type galaxies, but not rare. Polar ring galaxies, a rare breed of S0s with a ring of neutral hydrogen perpendicular to the galaxy's symmetry plane, have been used to constrain the mass and shape of DM halos, but much depends on the assumption of self-gravity of the ring (Sparke 2002). The most consistent evidence for a DM halo around ellipticals comes from studies of their hot gas, which radiates in the X-ray around 1 keV. Using a sample of giant ($L > L_*$), ellipticals Loewenstein & White (1999) conclude that DM does not dominate within an effective radius, but that the DM fraction within $6R_e$ is in the range of 39-85%. Because

early type galaxies with $L < L_*$ have faint X-ray spectra which tend to be dominated by the contribution from the stellar component, e.g. X-ray binaries, this finding cannot be extended to fainter ellipticals. Imaging by X-ray satellites *Chandra* and *XMM-Newton*, which shows bubbles and other structures, has complicated the picture presented by Loewenstein & White (1999), which assumes—as is typical—sphericity and (isothermal) hydrostatic equilibrium. For a recent review of the topic of hot gas in ellipticals, see Mathews & Brightenti (2003).

Gravitational lensing of light by elliptical galaxies is an additional probe of DM halos, especially at large radii. Wilson et al. (2001) have used the distortion (shear) of faint background galaxies by a foreground galaxy to measure the mass-to-light ratio of early-type galaxies. Adding the shear signal from many hundreds of early type lens galaxies in their fields they derive $\Upsilon_B \sim 121 \pm 28$ within ~ 100 kpc. Strong lensing, where the lens galaxy produces multiple—typically two or four—images of a background source, yields more specific information, but the sample of lens systems is limited (< 50). Keeton (2001) deduces that DM cannot account for more than 33% of the mass within one R_e , or 40% within $2R_e$, consistent with the findings of Loewenstein & White (1999).

Finally, globular clusters (GCs), planetary nebulae (PNe), and satellite galaxies provide discrete tracers of a galaxy’s kinematics and, with suitable assumptions, of the dynamics (e.g., Romanowsky & Kochanek 2001). GCs are not as numerous as PNe, and the additional difficulty of absorption line spectroscopy on faint objects has limited the use of GCs as kinematic tracers (e.g., Bridges et al. 2003; Côté et al. 2003). The analysis is further complicated by the fact that GCs do not generally trace the light distribution of their host galaxy. In this paper we focus on the Planetary Nebulae (PNe) that can be used to investigate the dynamics of early-type galaxies. This approach stretches back to Nolthenius & Ford (1986) and their study of M32. PNe are part of the brief phase in the life of an intermediate mass ($0.8\text{--}8 M_\odot$) star when it evolves from a red giant to a white dwarf; this makes PNe a good tracer of old stellar populations (but see Peng et al. (2005) for a discussion on “young” PNe). During this transition the star ejects most of its mass, leaving a hot stellar remnant which rapidly ($\sim 10^4$ years) cools to a white dwarf. The PN proper is an expanding shell of dense gas being photo-ionized by the central stellar remnant. PNe are bright objects, emitting on the order of a few hundred L_\odot in a few emission lines, most notably [O III] $\lambda 5007$ (up to 15% of the total luminosity; Dopita et al. 1992). This not only enables us to detect them at extragalactic distances (out to 10–15 Mpc on 4-m class telescopes), but also to measure their velocity along the line of sight.

We have collected PNe samples for a set of early-type galaxies with the Rutgers Fabry-Pérot (RFP), which can be thought of as a narrow band (~ 2 Å) filter with a tunable central wavelength. Scanning around the (redshifted) [O III] $\lambda 5007$ emission line, the RFP generates a three-dimensional data cube where the galaxy background has been strongly reduced and monochromatic point sources, such as PNe, stand out against the background. Detection and measurement of the radial velocity are all achieved in one observing run. Other techniques that look for extragalactic PNe include the Planetary Nebula Spectrograph (Douglas et al. 2002), an instrument using slitless spectroscopy, and on/off band photometry in conjunction with multi-object spectroscopy (Peng et

al. 2004; Méndez et al. 2001).

The paper is outlined as follows: §2 summarizes the observing strategy and conditions; §3 and §4 discuss the data reduction and calibration; §5 to §7 show the process of our PN candidate selection, including accounting for completeness and interlopers; and we present the samples in full in §8. Considering the recent interest in NGC 3379 (Romanowsky et al. 2003) we present our mass models for this galaxy in §9. A summary of our findings is given in §10.

2. Observations

We observed the four galaxies in our sample with the RFP over the course of two runs at the CTIO 4 m Blanco telescope (f/8 Cassegrain focus). Details of the setup are given in Table 1. The RFP has a circular field of view with a diameter of 2'8, and a spectral response function that is well approximated by a Voigt profile with a FWHM $\simeq 2$ Å, equivalent to 120 km s⁻¹ at 5000 Å. There is a wavelength gradient between the center and the edge of an image of 4.6 Å. We typically scanned a wavelength span of 25 Å around the appropriately redshifted 5007 Å [O III] emission line in steps of approximately 1 Å. At this wavelength the free spectral range of the RFP is 48 Å and we used one of two blocking filters with a FWHM of 44 Å to ensure that only one order was transmitted. We used Tek 1024 × 1024 pixel CCDs, with 0'35 pixels (binned to 0'70 on the 1994 run), but only read out the portion of the CCD illuminated by the RFP.

At the start of each run we observed a set of emission lines around 5000 Å using a calibration lamp. The resulting “ring” images allowed us to establish the relationship between the gap setting z and the transmitted wavelength λ_c at the center of the image; to determine the free spectral range of the etalon; and to measure the shape of the spectral response function. To monitor changes in the wavelength calibration we took further images of the lamp throughout each night. We discuss the wavelength calibration in more detail in §4.2. For each run we obtained one series of dome flats at settings spaced ~ 1 Å apart. Twilight flats are not advisable, because of the spectral structure of the sky at the resolution of the RFP. Additionally we observed spectrophotometric standard stars on each run: six 90 s exposures of LTT 3218 in 1994 and six 300 s exposures of LTT 2415 in 1995 (Stone & Baldwin 1983).

The Leo galaxies, NGC 3379 and NGC 3384, were observed with multiple pointings, typically one pointing per night. NGC 1549 and NGC 4636, on the other hand, had only one pointing each, but were observed throughout the course of a run to get the full wavelength coverage. NGC 1549 was observed at the start of each night, NGC 4636 towards the end. The exposure time for each image was 900 s. To avoid systematic effects in the photometry consecutive exposures were not sequential in wavelength and were dithered by a few pixels. The appropriate blocking filter was determined by the central wavelength in an exposure being smaller or larger than the switching wavelength λ_s (see Table 1). Exposures were repeated if the seeing or the photometric conditions were particularly poor. The observations are summarized in Table 2.

The seeing was poor during both runs: $\sim 1.5''$ in 1995 and in the range $1.7\text{--}2.2''$ in 1994. The latter is partly due to difficulties in focusing the telescope and problems with the auto-guider. Conditions were mostly photometric in 1994, with the exception of the last half of the first night, which only affected the observations of NGC 4636. For the 1995 run we were less fortunate. The first two nights are fully photometric, but not the two following nights. As a result only half of our fields was observed completely under photometric conditions. As we will show below, this affected the quality of our PN photometry, but not of our radial velocity measurements.

3. Data Reduction

We used IRAF¹ for most of our data reduction. Each image was overscan corrected, trimmed and bias subtracted. Since the dark current contribution was negligible for the length of our exposures, no dark frames were taken. Each image was flatfielded using the flatfield image with a central wavelength closest to that of the image.

To aid the cosmic ray removal process and the photometry (see §4.3) we aligned the images for each pointing (a “stack”) using the few stars that were visible in each field (see Table 2). In all cases a simple shift over a few pixels proved to be adequate. Since the PSF was well resolved, we shifted the images by integer pixels to avoid interpolation effects. Cosmic rays were tagged, not removed, by combining all the images in a stack using the IRAF task `imcombine` with the `creject` rejection algorithm, creating a mask for each image which covered the cosmic ray events. To be conservative we added a rim of masked pixels around each event. The padded masks covered on average 8% of the field of view.

The final step in preparing the images in a stack was the removal of the background light. In our case the background is mainly light from the galaxy and its ghost, with the sky contributing an almost negligible amount. Ghosts are the result of the reflections between the CCD and the etalon, which create a faint in-focus replica of the original object, mirror reflected about the optical axis. We removed the background to reduce gradients which would bias the photometry, allowing us to detect PNe closer to the galaxy. We wrote a Fortran program which estimated the background with a ring filter (Secker 1995), where we replaced the median with a more robust estimator of the mean (Hoaglin et al. 1983). A ring filter removes objects at scales smaller than the diameter of the ring and we chose our diameter to be about twice the seeing radius. The shifted, masked and background subtracted stacks formed the basis for our further analysis.

¹IRAF is distributed by the National Optical Astronomy Observatories, which are operated by the Association of Universities for Research in Astronomy, Inc., under cooperative agreement with the National Science Foundation.

4. Calibration

The calibration of the RFP stacks consists of three parts: (i) image registration, i.e. assigning celestial coordinates to each pixel position; (ii) spectral calibration; (iii) flux normalization, i.e. accounting for variations in the observing conditions.

4.1. Image Registration

In each field we had only a few stars to register the images (see Table 2). These astrometric reference stars generally did not have published positions, because of their proximity to the galaxy being observed, and we had to determine their coordinates from observations with a larger field of view. For NGC 3379 and NGC 3384 we had deep broad band (V -like) images with $0''.4$ pixels; for NGC 1549 and NGC 4636 we used images from the Digitized Sky Survey² (DSS) with $1''.7$ pixels. Using the USNO-A2.0 catalog (Monet et al. 1998) we were able to identify 80 or more stars in each of these images and consequently measured the celestial coordinates of the RFP reference stars.

The systematic uncertainty in a single RFP coordinate, as estimated from the variance in the reference star positions, is $0''.6$ for NGC 1549 and NGC 4636, compared to about $0''.1$ for the other two galaxies. In the case of the Leo I galaxies (NGC 3379 and NGC 3384) we noticed a systematic $\sim 1''$ offset between the Ciardullo et al. (1989) coordinates and our own when we compared our PNe sample with their lists (see §8.3). We found that the offset can be attributed completely to the difference in astrometric reference star coordinates. Since our project does not require absolute astrometry we did not investigate the matter further.

4.2. Spectral Calibration

The transmitted wavelength λ at a position $\mathbf{x} = (x, y)$ on an RFP image taken at a gap setting z is given by

$$\lambda(x, y, z) = (a + bz)(1 + |\mathbf{x} - \mathbf{x}_c|^2/f^2)^{-1/2}, \quad (1)$$

where a and b are parameters relating z to the central wavelength of an RFP image, \mathbf{x}_c is the position of the optical axis of the RFP and f is the focal length of the camera lens of the RFP. To calibrate this relation we observe several emission lines from a calibration lamp at a range of z settings at the beginning of a run. During a run we take additional calibration images (“night rings”), eight to ten per night, to ensure the stability of our calibration. Over the course of our runs

²The Digitized Sky Survey was produced at the Space Telescope Science Institute under U.S. Government grant NAG W-2166. The images of these surveys are based on photographic data obtained using the Oschin Schmidt Telescope on Palomar Mountain and the UK Schmidt Telescope. The plates were processed into the present compressed digital form with the permission of these institutions.

b and f were stable, consistent with our experience from other runs. The value for \mathbf{x}_c , however, fluctuates as a result of flexure in the spectrograph; likewise, the wavelength zero-point a shifts due to drift in the control electronics. The overall drift in a was a little larger than 1 Å over a run; the overall shift in \mathbf{x}_c never larger than 6 pixels during a night. We interpolated the values for a and \mathbf{x}_c for each image from the values obtained from the night rings. The uncertainty in λ due to the calibration is 0.05 Å (3 km s⁻¹ at 5007 Å), based on the scatter in our calibration fits with the dominant source of uncertainty being f .

The initial calibration run also allows us to calibrate the spectral response function (SRF) of the RFP, i.e. the line shape of a monochromatic source. Although for a perfect etalon the SRF is an Airy function, experience shows that the SRF is better fitted by a Voigt function, the convolution of a Gaussian with a Lorentzian (van de Hulst & Reesinck 1947). The shape is determined by two parameters: the Gaussian width $\Delta\lambda_G$ and the Lorentzian width $\Delta\lambda_L$ (see Table 1). Note that the shape parameters are significantly different between the two runs, but that the full width at half maximum (FWHM) of the profile is practically the same at ~ 2 Å. We intentionally did not want to resolve the intrinsic structure of the PN line profile (see Section 6.1), since it would reduce the depth of our survey and would complicate our study unnecessarily.

4.3. Flux Normalization

In each field of view we use a reference object to provide us with a fiducial flux for every image in a stack, to calibrate the extinction due to light cirrus. Considering the narrow wavelength range we are observing it is reasonable to assume a flat spectrum for each reference object. We can then calculate normalization factors for each image in a straightforward manner. Only the spectrum of the reference star in the West field of NGC 3379 showed an indication of absorption lines. For NGC 3379 we therefore decided to use the galaxy flux within a 10'' aperture as a reference source. The galaxy spectrum has a slight curvature at the blue edge, which we modeled with a smoothing spline. The uncertainty in each normalization factor is 3-5%.

We were unable to get an independent determination of the atmospheric extinction during our runs, because we observed our spectrophotometric standard stars only once a night and all at approximately the same airmass. Instead, we adopted a value for the extinction of 0.19 magnitude per airmass as given for CTIO (Hamuy et al. 1992); on photometric nights the flux normalization factors were found to be consistent with assumed extinction. Finally, using the spectrophotometry for the standard stars, we converted our instrumental fluxes to physical units. Comparison with previously published PN magnitudes shows no systematic effects (see below).

5. Extracting Spectra

We extract spectra for every independent point in the field of view of a stack and for each spectrum decide whether or not an emission line is present. A more targeted approach, where we would look for emission line point sources in each image of a stack using, for instance, DAOPHOT (Stetson 1987), requires extensive fine tuning due to the low signal-to-noise ratio of the objects and still produces numerous spurious detections. (Tremblay et al. (1995) used this approach to look for PNe around NGC 3384.) Our method is not computationally expensive and has no bias due to a search algorithm.

The fluxes for each spectrum were extracted using the `apphot` aperture photometry package in IRAF. We performed a set of Monte Carlo simulations of our instrumental setup (see Table 1) to compare the results of PSF and aperture photometry. PSF photometry, assuming perfect knowledge of the PSF, produced an appreciably larger scatter in the derived fluxes than aperture photometry did. Because we have only one star in each field bright enough to determine a PSF, there was the additional concern of the effects of a PSF mismatch. Both considerations lead us to use aperture photometry.

Each field of view was sampled on a triangular grid, the most isotropic choice. The spacing between sample points was chosen to Nyquist sample the image, i.e. sample points are separated by half the smallest seeing FWHM in a stack, to guarantee no information was lost. Following Naylor (1998) we chose our aperture radius to be slightly larger than two thirds of the seeing FWHM in order optimize the signal to noise ratio within the aperture. In this case the photometry apertures overlap slightly more than 50% in area. If the aperture contained masked pixels, e.g. a cosmic ray, the data point was removed from the spectrum. In cases where we measured a negative flux, we estimated the uncertainty from the uncertainties in the positive fluxes near the continuum level. No aperture corrections are needed, since we photometer a PN candidate and a reference star in the same way.

The final data product, then, is a set of M spectra where each spectrum is a list of the form $\{\lambda_i, f_i, \sigma_{f_i}, e_i\}_{i=1}^N$ with N the number of images in a stack, λ_i the wavelength, f_i the flux, σ_{f_i} the uncertainty in the flux and e_i a possible photometric error flag. In the following section we discuss how we determine which spectra indicate the presence of an emission line.

6. Candidate Selection

To establish the presence of a PN candidate in a spectrum we fit a flat continuum model and an emission line model to each spectrum, measuring the difference in the goodness-of-fit using a statistic S . After calibrating the distribution of S with Monte Carlo simulations we choose a significance level α and select all spectra with a value $S > S(\alpha)$. Finally, we visually inspect each stack at the candidate positions to verify the selection and avoid contamination from CRs and

image artifacts. The details of the procedure are described below.

6.1. Modeling the spectra

We expect most extracted spectra to have a flat, practically zero, flux distribution, since we removed the background in each image. In addition a flat model spectrum should encompass the spectra from foreground stars in our field. Hence, our null hypothesis is a simple constant flux model. Modeling spectra with a linear function $f_i = a\lambda_i + b$ yielded no significant improvements over the constant model, because of the flux uncertainties.

The alternative hypothesis is that a spectrum contains an emission line. Such a model needs to take into account the intrinsic structure of the [O III] line, since PNe, as observed in our own Galaxy, often have doubly peaked emission lines (Pottasch 1984). The intrinsic width of each of these peaks is small ($\sim 10 \text{ km s}^{-1}$), and the nebular expansion velocity v_{exp} , defined as half the separation between the two peaks, has a distribution with a mode around 10 km s^{-1} , but a mean of 25 km s^{-1} due to the large tail at higher velocities (Phillips 2002). Based on the latter we calculate that the broadening of our *observed* line profile (see below) due to line structure is $\lesssim 9\%$, negligible considering the wavelength sampling of our spectra (see Table 1). We will assume from now on that PNe can be treated monochromatic point sources.

Consequently, the line profile is determined by the effective filter transmission T and the RFP spectral response R_s . We separate the two because they are measured separately from each other. The measurement of the latter is described in section 4.2; for the former we use the filter curves provided by CTIO. We assumed that temperature effects on T are unimportant. The f/7.5 beam used for our observations is slow enough to have a negligible effect on the transmission properties of our filters (Ciardullo et al. 1989).

The effective filter transmission T changes the line shape from a simple Voigt profile in two ways. The first modification is a discontinuous jump in the emission line profile, which is the result of changing from the “blue” filter T_b to “red” filter T_r whenever the central wavelength of an image is larger than the switching wavelength λ_s . The total flux of a PN observed at λ_{pn} will differ between the two filters, since in general $T_b(\lambda_{\text{pn}}) \neq T_r(\lambda_{\text{pn}})$. Hence, a spectrum will show a jump at λ_s . The jump is appreciable when λ_{pn} close to λ_s , but is otherwise negligible.

The second modification stems from the fact that the flatfield images are based on exposures of continuum sources. A flatfield image taken on the red edge of a filter includes light from the neighboring order of the RFP on the blue edge. As a result we overestimate the sensitivity of the detector when applying the flatfield to an emission line object, which has flux in one order only. Ignoring this effect would lead to a wavelength dependent bias in the measured total flux of a PN. We can adjust for this effect by calculating a correction factor Γ , the integral over the filter transmittance and the SRF. Figure 1 illustrates how the two effects modify the line profile.

To account for the above two effects we characterize the spectrum of a PN candidate extracted from a stack of N images in the following way:

$$M(f_{\text{pn}}, \lambda_{\text{pn}}, c_{\text{pn}} | \mathbf{x}, z_i) = f_{\text{pn}} \frac{R_s(\lambda_{\text{pn}}, \mathbf{x}, z_i) T(\lambda_{\text{pn}}, z_i)}{\Gamma(\mathbf{x}, z_i)} + c_{\text{pn}}, i = 1, \dots, N, \quad (2)$$

where M is the flatfielded and normalized flux measured at position \mathbf{x} and RFP setting z_i , f_{pn} is the total flux received from the PN candidate, R_s is the SRF, $T(\lambda_{\text{pn}})$ is the appropriate filter transmission, and c_{pn} is the continuum level. Since the spectra we extract from the RFP stacks are critically sampled, we cannot constrain the shape of the line profile in addition to fitting a peak wavelength, total intensity and background flux. Hence, we fixed $\Delta\lambda_G$ and $\Delta\lambda_L$ to the values determined from the calibration run in our further data analysis. The factor $\Gamma(\mathbf{x}, z_i)$ corrects for the luminosity bias; it depends implicitly on R_s and T . Note that c_{pn} can potentially give us a handle on the contamination of our sample (see section 7.2).

We fit the two models to each spectrum by minimizing a goodness-of-fit statistic $s^2(f_{\text{pn}}, \lambda_{\text{pn}}, c_{\text{pn}})$ defined by

$$s^2 = \sum_{i=1}^N \frac{[f(\mathbf{x}, z_i) - M(f_{\text{pn}}, \lambda_{\text{pn}}, c_{\text{pn}} | \mathbf{x}, z_i)]^2}{\sigma_{f_i}^2}. \quad (3)$$

We set $f_{\text{pn}} \equiv 0$ for the continuum model and $f_{\text{pn}} \geq 0$ for the emission line model. The minimum s^2 value was found using the E04UNF routine from the NAG numerical library, which is designed to solve nonlinear least-squares programming problems in the presence of constraints on the parameters. Since the uncertainties in our data points are not gaussian, the uncertainties in our best fit parameter values do not necessarily correspond to a 1σ error. We used simulated observations (see Section 6.3) to verify the plausibility of uncertainties found in the fitting procedure.

6.2. Choosing the correct model

The continuum model M_c and the emission line model M_l are nested models, i.e. the parameters in M_c form a subset of the parameters in M_l (the additional parameters of M_l are fixed to some default value). The likelihood-ratio (LR) test or the F -test are conventionally used to decide between the null hypothesis M_c and the alternative hypothesis M_l (Eadie et al. 1971; Band et al. 1997). Each of these tests uses a test statistic S which is some simple function of \hat{s}_c^2 and \hat{s}_l^2 , the best fit values of s^2 for M_c and M_l , respectively. Under certain regularity conditions these test statistics have analytically known reference distributions (e.g. Protassov et al. 2002), usually in the limit of large N , which allow a level of significance to be determined for the observed value of S .

In our case two of the regularity conditions are not met. First, the tests assume that the data are independent, identically distributed random variables. As a result of the flatfielding the data points in our spectra are not identically distributed. Second, the default values for the additional

parameters in M_l cannot be on the boundary of parameter space. The null hypothesis assumes that $f_{\text{pn}} \equiv 0$, clearly on the boundary of our parameter space. This is not an academic point: Mattox et al. (1996) show that when this condition is violated the actual reference distribution is markedly different from the nominal reference distribution (see their Figure 3). The problem of including boundary values in a parameter space has no standard analytical solution. Protassov et al. (2002) present a more comprehensive introduction.

We decided to use the LR test statistic $S = \hat{s}_c^2 - \hat{s}_l^2$, but to calibrate its reference distribution by way of Monte Carlo simulations instead of using the nominal reference distribution. (The choice of the LR test over the F -test is motivated in the next section.) The reference distribution $p(S|M_c)dS$ specifies the probability that the test statistic has an observed value S under the condition that the null hypothesis is true. To calibrate $p(S|M_c)$ we simulated stacks of images that contain no emission line objects, preserve the noise characteristics of the original observations, and are reduced in the same way as the original observations. Every field of view was calibrated separately.

As an example, we show the result of these simulations for the East field of NGC 3379 in Figure 2. The nominal reference distribution of S in our case is a χ^2_2 distribution (Eadie et al. 1971). In this particular case the actual reference distribution can be approximated by a χ^2_ν distribution, as shown by the best-fitting $\chi^2_{4.6}$ curve, but this is not generally true. A proper calibration of the test statistic is clearly essential in order to avoid a plethora of false positives. For each field of view we choose the value of $S_c(\alpha)$ that corresponds to a significance level $\alpha = 0.01$ and select all spectra with $S > S_c(\alpha)$. Our experience shows that at this significance level we can observe a PN candidate in at least two frames.

6.3. Final selection

Since the photometric apertures overlap, PNe candidates in each field of view tend to cluster in contiguous groups of 3-6 spectra sharing a similar central wavelength λ_{pn} . Instead of developing an algorithm to make a final selection of candidates from these clusters, we performed the final selection by hand. First we remove any obviously false identifications due to CRs and image artifacts, e.g. the ghost image of a bright star. Next we choose the brightest spectrum in a cluster as the candidate spectrum and visually inspect its position in every image of the stack. Once we are convinced we have a bona fide PNe candidate, we determine the exact position of the candidate and redo the photometry of the candidate to provide the final parameters for the object.

We have two estimates for the uncertainties in f_{pn} , λ_{pn} , and c_{pn} : the variances from the formal best-fit covariance matrix (Eadie et al. 1971), and the empirical estimates from the artificial PNe simulations (see section 7). For PN candidates with $S > S_c(\alpha)$ we found that the best-fit parameters are only slightly correlated and that the two uncertainty estimates are consistent with each other. Hence, we used the best-fit variances as our measure of the uncertainties in the magnitude and line-of-sight velocity. We note that λ_{pn} is in our experience significantly better constrained than f_{pn} ;

the continuum level c_{pn} is always consistent with zero, as expected. The false-negative simulations also allow us to estimate the random uncertainty in a PN position at $0''.3$, which does not include the systematic uncertainty discussed in section 4.1.

In the same way that one can determine an aperture radius that optimizes the signal-to-noise ratio Q within some photometric aperture (Naylor 1998), we determine a wavelength window centered on the peak wavelength which optimizes Q in the spectral domain. Numerical experiments show that a window width of $4/3$ the spectral FWHM is optimal. To calculate the signal-to-noise ratio we simply added the signal from all frames within 1.4 Å of λ_{pn} and divided this by the sum in quadrature of the uncertainties (all quantities were converted to photons). Taking into account the seeing, the background flux, the sampling and the photometric conditions of our observations, we find that our empirical values are in agreement with the theoretical expression of Douglas et al. (2002, eq. 6).

7. Completeness and Contamination

To characterize our PN samples fully we need to address two issues: completeness and contamination. The former describes the probability that our experiment, i.e. the whole of observations, data reduction and analysis, would not detect a PN with a flux f_{pn} . The latter specifies the extent to which candidates in our samples are not actually PNe. In the context of our experiment the completeness is closely related to the (statistical) power of the test statistic and we show that the LRT is preferred over the F -test because it gives us a more complete sample. It is more difficult to quantify the contamination, mainly because the distribution of possible contaminating sources is still poorly understood. Based on our estimates, discussed in more detail below, contamination is not a serious concern in our samples.

7.1. Completeness and power

For statisticians the usefulness or *power* of a test lies in its ability to reject the null hypothesis ($f_{\text{pn}} = 0$) when in fact the alternative hypothesis ($f_{\text{pn}} > 0$) is true.³ The power function $\beta(f_{\text{pn}})$ is quantified by

$$\beta(f_{\text{pn}}) = p(S < S_c(\alpha) | f_{\text{pn}}), \quad (4)$$

i.e. the probability that, given a level of significance α , we reject the true (alternative) hypothesis (Eadie et al. 1971). The actual form of $\beta(f_{\text{pn}})$ is contingent upon our choice of α , but is generally monotonically increasing. When multiple tests are available, statisticians look for the test with a minimum $\beta(f_{\text{pn}})$, the one least likely to lead to an invalid conclusion.

³For purposes of detection, λ_{pn} and c_{pn} are parameters of little interest (“nuisance parameters”) and we marginalize the distribution of S over these two parameters.

Astronomers, on the other hand, think in terms of completeness: we want to maximize our ability to identify objects of a given type. Since our experiments are limited by observing conditions (exposure time, seeing, etc.) we rarely obtain a complete sample, instead quantifying the level of completeness in terms of a limiting magnitude. Typically, the depth of a survey is defined by the flux level where the probability of detecting an object is 50%: $\beta(f_{\text{lim}}) = 0.5$ (Harris 1990). Hence, the more powerful test is the test where f_{lim} is the smallest and so allows the survey to go deepest.

We considered two statistics commonly used in model comparisons: the LR statistic

$$S_{\text{LR}} \equiv \hat{s}_c^2 - \hat{s}_l^2, \quad (5)$$

and the F -statistic

$$S_F \equiv \frac{s_c^2 - s_l^2}{s_l^2} \Big/ \frac{N - \Delta P}{P_l}, \quad (6)$$

where N is the number of data points in a spectrum, $P_l = 3$ the number of parameters in M_l , and $\Delta P = 2$ the difference in the number of parameters between M_c and M_l . A third statistic that is sometimes used, the Goodness-Of-Fit statistic $S_{\text{GOF}} \equiv \hat{s}_c^2$, was not considered, since it does not take into account an alternative hypothesis and consequently is not a powerful test. Although S_{LR} and S_F yield about the same significance for a spectral feature (Band et al. 1997), the LR test is generally more powerful than the F -test, the latter being the more appropriate test when the uncertainties in the data are unknown (Freeman et al. 1999).

In order to ascertain the limiting magnitude of our observations we simulated stacks with artificial PNe and analyzed them as we would real observations. By comparing the analyses using S_{LR} and S_F we found that the former is the more powerful of the two tests, as expected. An illustration of this point is given in Figure 3: in the case of our NGC 3379 observations S_{LR} allows us to go ~ 0.3 mag deeper than S_F . The limiting magnitudes for each field of view are shown in Table 2.

7.2. Sources of contamination

Each PN detection is based on the assumption that the detected emission line is the [O III] 5007 line. A simple way to check if a candidate is actually a PN, short of taking a complete spectrum, is to measure the flux in the [O III] $\lambda 4959$ emission line, since the line ratio $I(5007)/I(4959) = 3$ is fixed (Freeman et al. 2000). Our wavelength range, however, does not include the redshifted $\lambda 4959$ line, and we have to rely on statistics to appraise the possibility of an interloper in our PN samples.

The search for high-redshift emission line galaxies in order to determine their star-formation history (Hu et al. 1998; Stern et al. 2000), as well as searches targeted to quantify the contamination of intracluster PN surveys (Kudritzki et al. 2000; Ciardullo et al. 2002) have improved our understanding of possible contaminants. The most likely candidates that—to our

knowledge—could contaminate our samples are Ly α sources at $z = 3.13$, and [O II] $\lambda 3727$ at $z = 0.35$ (Kudritzki et al. 2000). In the absence of any other information, the most likely interloper is a Ly α source, since these tend to have significantly stronger lines than the [O II] sources (Ciardullo et al. 2002). In particular, at the depth of our observations ($m_{5007} < 26.6$ or $f_{5007} > 0.7 \times 10^{-16}$ erg cm $^{-2}$ s $^{-1}$) the probability of the latter contaminating our samples is negligible. For the former Ciardullo et al. (2002) determine a surface density of ~ 3500 deg $^{-2}$ per unit redshift for Ly α with $f_{5007} > 0.5 \times 10^{-16}$ erg cm $^{-2}$ s $^{-1}$, consistent with the determination of Castro-Rodríguez et al. (2003) for the Leo group of galaxies. Taking into account the redshift range ($\Delta z \sim 0.005$) and the effective area (5.8–16.2 arcmin $^{-2}$) of our surveys, we expect well fewer than one contaminating source in any of our samples.

The estimate does not take into account any clustering of the background sources anticipated because of large scale structure, which could result in significant fluctuations in the surface density (Ouchi et al. 2003). In many cases, however, the Ly α line will be broad enough to be resolved by the RFP and have an asymmetric profile (e.g., Castro-Rodríguez et al. 2003). Such sources are unlikely to be selected in our detection procedure and would be recognizable from their spectra. Additionally, these Ly α sources often have a faint continuum which can be used to identify an interloper, which partly motivated our inclusion of a continuum term in equation 2. All our candidate spectra show continuum levels fully consistent with a zero background. On the basis of these considerations we believe that the possibility of contamination by Ly α sources in our samples can be ignored.

8. Results

Our galaxy sample consists of three close to round elliptical galaxies and one lenticular galaxy. An overview of the properties of our galaxy sample is given in Table 3. We present the spectra for each PN in our samples, as well as tables with positions, magnitudes, and line-of-sight velocities. A simple overview of the line-of-sight velocities for all four galaxies is shown in Figure 4.

8.1. NGC 4636

The E1 galaxy NGC 4636 lies on the Southern edge of the Virgo cluster and has been well studied because of its high X-ray luminosity. Ravindranath et al. (2001) note that the galaxy does not follow the Fundamental Plane relation for core galaxies (its surface brightness is too low for its absolute luminosity) and has an unusually diffuse core. This is reflected in the large effective radius of the system.

All the NGC 4636 images were taken at the end of each night during the 1994 run. Of the 34 available image 28 were centered on the galaxies, but 6 were offset by half a field radius. Additionally, the seeing of these observations was large (2''.2) and the first night we had non-

photometric conditions. Because of the lower surface brightness we were able to go deep enough to discover two PNe in this system, whose velocities are consistent with the systemic velocity (McElroy 1995). The spectra are shown in Figure 5.1 and the properties of the PNe in Table 4.

8.2. NGC 1549

The E1 galaxy NGC 1549 is in close interaction with its neighbor NGC 1553 as is evidenced by the strong isophote twisting (Franx et al. 1989) and the faint shells surrounding it (Malin & Carter 1983). The galaxy is the most distant in our sample and has not been targeted for a PN survey before. Photometric conditions varied throughout the five nights of observation, but this was mitigated by the relatively good seeing and the small airmass of the observations, which allowed us to go a little deeper than for the Leo galaxies. The galaxy was observed with one pointing, giving an effective survey area of 5.8 arcmin^{-2} . We discovered 6 PNe around this galaxy. The spectra are shown in Figure 5.1 and the properties of the PNe in Table 4. Their average velocity of 1279 km s^{-1} is consistent with the 1220 km s^{-1} systemic velocity of the galaxy and their velocity dispersion $\sigma = 217 \text{ km s}^{-1}$ matches the value found with absorption line spectroscopy (220 km s^{-1} , Longo et al. 1994).

8.3. NGC 3379

The E1 galaxy NGC 3379 (M105) forms with NGC 3384 (below) the central pair of the Leo (M96) group (Ferguson & Sandage 1990). Following the work by de Vaucouleurs & Capaccioli (1979) NGC 3379 is often considered the “standard” elliptical, although Capaccioli et al. (1991) have argued, purely on the basis of photometry, for a reclassification from E1 to S0. Because of its proximity NGC 3379 is an ideal candidate to look for extragalactic PNe and we observed it with two pointings, giving an effective survey area of 11.9 arcmin^{-2} , which excludes the bright central ($< 10''$) part of the galaxy. The frames for each pointing were taken over two nights; each pointing had one night of non-photometric quality. Because one of our reference stars showed evidence of an absorption line in its RFP spectrum, we used the galaxy flux within $0.5R_e$ as the photometric reference for our flux normalization. We present our sample of PNe in Table 5; the corresponding spectra are shown as Figures 5.2–5.4 in the online version of the Journal.

In NGC 3379 we find 54 PNe out to $\sim 5R_e$. The sample is sparse and its distribution on the sky is consistent with the surface brightness of NGC 3379, taking into account the position dependent limiting magnitude. Using the on/off band technique Ciardullo et al. (1989) obtained a sample of 93 PNe in NGC 3379. In a spectroscopic follow up Ciardullo et al. (1993) measured the line-of-sight velocities of a subset of 29 PNe. In principle we can observe 57 of the Ciardullo et al. (1989) candidates, and we recovered 30 of these. Similarly, we can measure 15 velocities from Ciardullo et al. (1993) and we recover 7 of these. The overlap with the previous work gives

us an independent check on our calibration: comparisons of the PN magnitudes and line-of-sight velocities are shown in Figures 6 and 7. The magnitudes are consistent within their uncertainties, although there is clearly crowding near the limiting magnitudes of either survey. Considering that 50% of our data was taken under non-photometric conditions, the agreement is remarkable. The additional tight agreement between the two velocity measurements further convinces us that we calibrated our data properly and adequately.

In our sample of PNe we have one candidate with an unusual velocity: E27 at 291 km s^{-1} . It is unlikely to be associated with NGC 3384, because of the latter’s velocity field, which would favor PNe with velocities over 720 km s^{-1} . Hence, it could either be an interloper or an intragroup PN, but we have no way of ascertaining either conjecture. In the mass models we present for NGC 3379, we exclude this object in our data analysis.

The overall pattern of radial velocities (see Fig. 4) shows the signature of minor axis rotation. Although there are not enough data points for an informative independent estimate of the velocity field based on the PNe alone, simple smoothing spline estimates of the rotation and velocity dispersion (using code kindly provided by D. Merritt) are consistent with the long slit results of Statler & Smecker-Hane (1999), yielding $V/\sigma \sim 0.25$. Hence we can apply the Tracer Mass Estimator (TME; Evans et al. 2003) to give a first approximation of the total mass of NGC 3379. Assuming a number density $n \propto r^{-2.3}$ and a logarithmic potential, the TME yields $(2.1 \pm 0.1) \times 10^{11} \text{ M}_\odot$ within 8 kpc, where the uncertainties were derived assuming anisotropies $\beta = \pm 0.3$. The implied B band mass-to-light ratio is $\Upsilon_B = 9.9 \pm 0.5$.

8.4. NGC 3384

The SB0 galaxy NGC 3384 is the closest companion of NGC 3379 and is one of the brightest members of the Leo (M96) group (Ferguson & Sandage 1990). There is some evidence for interaction from a faint tidal arm (Malin 1984) and the large HI ring that surrounds the galaxy pair (Schneider 1989). Three components contribute to the light distribution of NGC 3384: a small bulge with a complex structure which includes the bar within $\sim 20''$, a lens that extends out to $160''$ and an outer exponential disk (Busarello et al. 1996). The galaxy was also observed by Ciardullo et al. (1989), who found a sample of 102 PNe (100 if we identify two pairs of PNe separated by less than $0.5''$). There was, however, no spectroscopic follow up for their NGC 3384 sample.

NGC 3384 was observed with four pointings, giving an effective survey area of 16.2 arcmin^{-2} , which excludes the bright inner part of the galaxy, ghosts, and the brightest reference stars. Because the RFP produces ghost images of bright objects the survey area has a complicated topology; spectra will have as few as 19 data points in some regions and as many as 65 data points in others. We purposely avoided the region between NGC 3384 and NGC 3379. The galaxies have systemic velocities that are close enough to make it impossible to disentangle the correct host of each PN candidate in the intergalactic area, even more considering the possible interaction between the two.

The NGC 3384 data have been discussed previously by Tremblay et al. (1995), but was based on a different data reduction and candidate selection process. We present our sample of PNe in Table 6; the corresponding spectra are shown as Figures 5.5–5.7 in the online version of the Journal.

With our field of view we can, in principle, observe 82 PNe from the Ciardullo et al. (1989) sample. We recover 37 PNe and discovered 13 new PNe. The comparison of the magnitudes of the PNe we have in common is shown in figure 8. As before, the agreement is quite good. An interesting candidate is W05, the outlier at the bright end of the plot. Visual inspection shows possible structure around this candidate. Ciardullo et al. (1989) interpreted this as two close candidates (their numbers 6 and 60), which seems unlikely since the two candidates are close both in velocity space and on the sky. Hence, W05 could be an interloper, but we include it for completeness.

We can apply the TME to the NGC 3384 data, but we need to make some additional assumptions, since Figure 4 shows the clear disk-like kinematics of the PN sample. We will assume that the S0 has a flat rotation curve at 120 km s^{-1} and that all PNe lie in the plane of the disk with a power law density distribution. The disk has a presumed inclination $i = 62^\circ$; hence we can split the line-of-sight velocities of the PNe into a component due to the rotation and a random component. We apply the TME to the random component, adding $\langle v_{\text{rot}} \rangle r/G$ for the rotational motion to arrive at the total mass: $(5.1 \pm 0.3) \times 10^{10} \text{ M}_\odot$ within 9 kpc. The implied B band Υ_B within this radius is 10.9 ± 0.7 .

9. Mass modeling

9.1. Physical Framework

Determining the potential of a spherical system, let alone an axisymmetric or triaxial system, using a discrete kinematic tracer population such as PNe would take on the order of 10^3 radial velocities (Merritt & Saha 1993). With our samples ($N \lesssim 50$) clearly falling short of this requirement, we shift the objective of our modeling from finding the most likely mass model to assessing the constraints the PNe velocities can place on the distribution of mass at $r \gtrsim R_e$. Only the two Leo galaxies, NGC 3379 and NGC 3384, have PN sample sizes that are large enough to give potentially interesting results. In the following we consider spherical mass models for the E1 galaxy NGC 3379; attempts to build axisymmetric mass models for the S0 galaxy NGC 3384 were not successful and are not presented here (Sluis 2004).

Our model space M is predicated on the Jeans equation for a spherical non-rotating system, assuming a distribution function of the form $f(E, L^2)$:

$$GM_<(r) = -r\sigma_r^2(r) \left(\frac{d \ln \nu}{d \ln r} + \frac{d \ln \sigma_r^2}{d \ln r} + 2\beta(r) \right), \quad (7)$$

where $M_<(r)$ is the mass interior to radius r , $\nu(r)$ the luminous density of the tracer population,

$\sigma_r(r)$ the radial velocity dispersion of said population, and $\beta(r) \equiv 1 - \sigma_t^2(r)/\sigma_r^2(r)$ its velocity anisotropy. The gravitational potential of NGC 3379, an E1 galaxy, will be rounder than its mass distribution (Binney & Tremaine 1987) and deviate from sphericity by only a few per cent. Because the PNe data sets are highly incomplete within $1 R_e$ we augment our kinematic data with the results of long slit spectroscopy to constrain the models in the inner regions, assuming both data sets represent the same tracer population. In the case of NGC 3379 we will use the results of Statler & Smecker-Hane (1999). The kinematic data show an amount of rotation ($V/\sigma \sim 0.25$) that is slight enough to reasonably model the galaxy as a non-rotating system.

We derive the luminous density $\nu(r)$ from the surface brightness $\mu(R)$ by applying an Abel inversion in the fashion of Gebhardt et al. (1996). For the surface brightness $\mu_B(r)$ we combined the groundbased data from Peletier et al. (1990) with the *HST* data (F555W filter) from Gebhardt et al. (2000) shifted to B band by assuming a uniform color (Goudfrooij et al. 1994). The combined surface brightness profile only extends out to $154''$, and we performed a linear extrapolation in $(\log r, \mu_B)$ for larger radii.

9.2. Exploring the model space

In looking for ways to analyze the range of plausible mass models for NGC 3379, we insisted that our method be non-parametric and use the data directly. A non-parametric method, though generally computationally intensive, will give a more conservative estimate of the range of possible mass models and will come closer to the most likely model than a parametric method. Indeed, the form of a parametric function can artificially constrain our search for plausible mass models. Furthermore, we want to be frugal with our data and avoid unnecessary binning of the PNe velocities. In other words, instead of relying on the unstable process of estimating and differentiating $\sigma_r^2(r)$ to infer $M_<(r)$ from Equation 7, we posit $M_<(r)$ and measure its success in matching the observed data.

The method developed by Magorrian & Ballantyne (2001, MB), which is briefly reiterated below, meets both these requirements. The MB analysis is Bayesian in outlook and quantifies the plausibility of a mass model M given the data D :

$$p(M|D) \propto p(D|M)p(M), \quad (8)$$

where the “prior” probability $p(M)$ encodes our prejudices about the most appropriate model M absent any observations, the likelihood (“chi-squared”) $p(D|M)$ quantifies the probability of observing the data D given a model M , and the “posterior” probability $p(M|D)$ quantifies the distribution of plausible models M given our prejudices and the data. Credible regions—the Bayesian analog of confidence regions—are naturally constructed from the posterior and quantify the constraints the data place on the mass distribution.

We specify our models as follows. Given a *local* mass-to-light profile $\Upsilon(r)$ to convert the

luminous density $\nu(r)$ to a mass density $\rho(r)$, and an anisotropy profile $\beta(r)$ to determine $\sigma_t^2(r)$ from $\sigma_r^2(r)$, we can assay the likelihood $p(D|M)$ of the kinematic data by integrating equation 7 to find the velocity dispersion along the line of sight. (In the case of the long slit data the projected velocity dispersion is convolved with a Gaussian to mimic the effect of seeing.) The shape of $\Upsilon(r)$ is specified in terms of its values Υ_i at a discrete set of sample points $r_i, i = 1, \dots, N_\Upsilon$, with intermediate values obtained through interpolation. On the other hand, we will assume that the anisotropy is constant with either $\beta = 0$ or $\beta = 0.3$, partly for ease of computation, partly due to the work by Gerhard et al. (2001, fig. 4) who find a remarkably constant anisotropy ($\beta = 0.3$) in their dynamical models of giant ellipticals.

Having specified the projection of our model into observable space, we calculate the posterior probability $p(M|D)$ for a given trial model $M = \{\Upsilon(r), \beta\}$ from the likelihood and the prior probability. We define the likelihood as follows

$$\begin{aligned} \ln p(D|\Upsilon(r), \beta) = & -\frac{1}{2} \sum_i \left(\frac{\sigma_i - \sigma_p(R_i)}{\Delta\sigma_i} \right)^2 \\ & - \sum_j \left(\frac{v_j^2}{2\sigma_p^2(R_j)} - \ln \frac{\Delta v_j}{\sigma_p(R_j)} \right), \end{aligned} \quad (9)$$

where σ_i and $\Delta\sigma_i$ are the observed velocity dispersions from the long slit spectra and their uncertainties, and v_j and Δv_j are the radial velocities of the PNe and their uncertainties. The first term quantifies the goodness-of-fit for the long slit data and the second term quantifies the likelihood of a radial velocity v_j given the velocity dispersion along the line of sight. The prior probability of a trial model is in essence a smoothness constraint:

$$\ln p(\Upsilon(r), \beta) = -\lambda \int \left[\frac{d^2(\ln \Upsilon)}{d(\ln r)^2} \right]^2 d(\ln r), \quad (10)$$

where λ specifies the amount of smoothness we prefer in our trial $\Upsilon(r)$. The prior gives a high probability to mass-to-light profiles that are close to a power-law, i.e. $\Upsilon(r) \sim r^\alpha$. In our experience the results of our calculation are not very sensitive to the value of λ : we settled on $\lambda = 0.1$. Nor is the value critical, since it simply encoded our prejudice as to what constitutes $\Upsilon(r)$ with too much variation. The next step is to investigate the posterior $P(M|D)$.

At this point we deviate from the MB method. Where they continue and include an ansatz for the distribution function of the system to ensure that the choices for $\Upsilon(r)$ correspond to a physical, i.e. non-negative, distribution function, we decided to forego this step in order to speed up the calculations. Our results might not always be physically plausible, but they are conservative, in the sense that the physical results are at worst a subset of our results.

The high dimensionality of our model space ($N_\Upsilon = 12$) precludes sampling the posterior $p(M|D)$ using a simple grid. Instead we explore the model space using a Monte Carlo Markov Chain (MCMC) method. A MCMC is no more than a random walk which, given enough steps, yields a set of trial models whose density distribution in the model space is proportional to the

posterior distribution. The main difficulty in using MCMCs is to ensure that the random walk has wandered enough through model space for the density of trial models to have converged to the posterior distribution. To improve the convergence of our MCMCs we use the slice sampler (Neal 2003) to generate the random walk instead of the more conventional Metropolis algorithm (Metropolis et al. 1953). Lacking a consensus among statisticians about the correct way to establish the convergence of an MCMC we use graphical checks of the random walks as well as the Gelman & Rubin R statistic (see, e.g., Verde et al. 2003). For a more detailed description of our implementation we refer the reader to Sluis (2004).

9.3. The results

We performed two sets of MCMC calculations: one for isotropic ($\beta = 0$) mass models and one for radially anisotropic ($\beta = 0.3$) mass models. In both cases we sampled $\Upsilon(r)$ at $N_\Upsilon = 12$ logarithmically spaced radii. We performed some exploratory calculations with a range of values for N_Υ . Our chosen value reflects the balance between an adequate resolution of $\Upsilon(r)$ and a reasonable convergence speed of the MCMCs. The MCMC for the isotropic models required a total of 1.8×10^5 iterations to converge; the anisotropic models a total of 4.6×10^5 . In both cases we discarded a total of 2×10^4 iterations as a “burn in” period for the chains. Once we have our set of trial models it is straightforward to establish the, e.g., 95% credible region for a given Υ_i by determining the range in Υ_i that encompasses 95% of all the trial models. Implicit in this determination is the marginalization of the posterior probability over all the other $\Upsilon_j, j \neq i$. Likewise we calculate the corresponding confidence regions for, say, $\sigma_p(R)$ and gauge how well our models can match the data. The results of our calculations are summarized in Figure 9 with credible regions of 99%, 90%, and 50%.

To provide some context we obtained the best-fit models for three parametric mass models: a Hernquist density profile $\propto r^{-4}$ (Hernquist 1990), an NFW profile $\propto r^{-3}$ (Navarro et al. 1997), and a pseudo-isothermal profile $\propto r^{-2}$ (Binney & Tremaine 1987), where in all cases $r \gg r_s$ with r_s the appropriate scale length; all three models have a second parameter ρ_s that scales the density. The best-fit models maximize the likelihood of the data—defined in Equation 9—by varying $M_<(r|r_s, \rho_s)$, but keeping $\nu(r)$ fixed, i.e. we do not assume a constant mass-to-light ratio for these models. They appear as the (red) curves in Figure 9.

The bottom panels of Figure 9 show that the non-parametric description of $\Upsilon(r)$ has more leeway than the parametric models in matching the actual data, especially around 1 kpc where the two sides of the galaxy have significantly different velocity dispersions and at the outer edges, where the PNe show a steep drop in velocity dispersion. We emphasize that our method does not bin the PNe velocities; the figure shows binned PN data for clarity. The core radii of the parametric models are quite small, an indicator of the failure of these mass models: the anisotropic Hernquist model has the largest scalelength with 0.6 kpc, the pseudo-isothermal model the smallest with 1.15 pc. A pseudo-isothermal profile, unsurprisingly, is not able to reproduce the data, because of its nearly

constant velocity dispersion; the Hernquist and NFW profiles do better, but still show a clear bias, justifying our choice for a non-parametric approach.

The difference between the two sets of models, at least in terms of matching the data, is a widening of the credibility contours in the case of the anisotropic models. (The results from MB for NGC 3379 in their Figure 3 show a similar widening.) Whether or not this is a significant difference can be answered by calculating the odds ratio (see Equation 14 of MB) of the isotropic versus the anisotropic hypothesis:

$$O = \frac{p(\beta_1|D)}{p(\beta_2|D)} = \frac{p(\beta_1)}{p(\beta_2)} \frac{\int p(D|\Upsilon, \beta_1)p(\Upsilon)d\Upsilon}{\int p(D|\Upsilon, \beta_2)p(\Upsilon)d\Upsilon}. \quad (11)$$

Typically, an odds ratio $O \sim 10$ is considered to be conclusive in favoring one hypothesis over another. Since we do not have any *a priori* preference for the value of β , the odds ratio reduces to the ratio of the average values of the posterior distributions. In the case of the parametric models $O \sim 2$, implying either hypothesis is equally likely. From the MCMCs we find $O = 4.6$ in favor of isotropy, which is a hint, but hardly conclusive. As MB noted, this is not a surprising result: barring information about the higher order velocity moments $\Upsilon(r)$ has enough freedom to match to data, given some value (or even profile) for β . The little information of these higher order moments encoded in the PN velocities is clearly not enough to be a useful discriminant.

The circular velocity in both sets of models is flat between 1 and 4 kpc at roughly 250 km s^{-1} , but drops off rapidly outside the latter radius, matching the results of Kronawitter et al. (2000, Figure 18). The agreement with the analysis of MB is less convincing at large radii, a consequence of their use of the smaller Ciardullo et al. (1993) PN sample. The largest difference between the two sets is within 0.6 kpc, where the anisotropic models need significantly less mass than the isotropic models to produce the same velocity dispersion profile. This is simply a reflection of degeneracy between mass and velocity anisotropy, which can only be broken by the inclusion of higher order moments velocity data (see Merritt 1993; Gerhard 1993; van der Marel & Franx 1993).

The top panels of Figure 9 show a constant $\Upsilon(r)$ between 0.1 and 2 kpc, before showing a small hump followed by a steep decrease at larger radii. The range in $\Upsilon(r)$ is consistent with the range found by Gerhard et al. (2001) for NGC 3379 from stellar population synthesis. The bump is related to the diverging velocity dispersion data points outside 1 kpc and creates a small plateau in the model velocity dispersion. The flaring of the $\Upsilon(r)$ credibility contours shows that the constraints on the mass-to-light profile from the PNe are weaker than those from the long slit spectra, but are nonetheless informative within 10 kpc. Compare the parametric models with their associated mass-to-light profiles: they agree fairly well with $\Upsilon(r)$ within 1 kpc (long slit spectra), but diverge strongly in the region dominated by the PN data. Despite this fact, the parametric models only allow us to conclude that the mass density should fall off steeper than $\propto r^{-2}$, but cannot discriminate between a Hernquist or an NFW profile. The non-parametric estimate $\Upsilon(r)$, however, not only matches the data better, but also gives us hints of a breakdown of our assumptions (a plateau instead of a flaring of confidence contours). Most remarkable, however, remains the relative flatness of $\Upsilon(r)$. The implied total mass within 8 kpc is $7.5 \times 10^{11} \text{ M}_\odot$, a factor of a few smaller

than the TME estimate in section 8.3. The total mass-to-light ratio implied is $\Upsilon_B \sim 7$, consistent with the stellar population models of Gerhard et al. (2001).

9.4. Discussion

The conclusion that our data show little evidence for DM in the inner 8 kpc of NGC 3379 is hardly surprising in the light of the work done by Ciardullo et al. (1993), Kronawitter et al. (2000), and—more recently—Romanowsky et al. (2003). In particular, a cursory inspection of the PN data in Figure 3 of Ciardullo et al. (1993) shows a striking resemblance to the similar data in our Figure 9: a steep drop off in velocity dispersion between $1R_e$ and $3R_e$. Using a parametric model that guaranteed a positive distribution function they found no significant signature for the presence of DM within $3.5R_e$ with $M = 1 \times 10^{11} M_\odot$ and $\Upsilon_B \sim 7$ consistent with our own findings. The investigations by Kronawitter et al. (2000), based on absorption line spectra out to $\sim 2R_e$, arrive at the same but more general conclusion: ellipticals likely have nearly maximal mass-to-light ratios. Specifically, they find $\Upsilon_B = 4.5$.

On the basis of orbit superposition modeling Romanowsky et al. (2003) determined a mass-to-light ratio for NGC 3379 in the B band of 7.1 ± 0.6 . Their sample included about ~ 100 PNe and also showed the radial decline in velocity dispersion. Indeed, they found the same decline in three more galaxies and concluded that elliptical galaxies contain little DM when compared to other galaxies. Considering the range in modeling procedures employed to study the dynamics of NGC 3379 and the consistency of the results, it is fair to say that it shows no evidence for dark matter within the inner few effective radii. At the same time, analysis of the HI ring around NGC 3379 and NGC 3384 implies an enclosed mass of $\sim 6 \times 10^{11} M_\odot$ (Schneider et al. 1989). The discrepancy between the total dynamical mass-to-light ratio $\Upsilon_B = 27$ within the 110 kpc ring (Schneider 1989) and within a 10 kpc radius of NGC 3379 suggests that most of the dark matter is at large radii.

Our models might not capture the complexity of NGC 3379 acceptably. The galaxy is not perfectly spherical and might even be an S0 seen face on (Capaccioli et al. 1991), but as Romanowsky et al. (2003) have observed, either possibility is unlikely to have a large effect on our final answer. The fact, noted by Statler & Smecker-Hane (1999), that the long slit data show a bump in the h_3 moment at $\sim 15''$ is interesting in this regard as an indication of a more complex description for NGC 3379 than incorporated in our model. The twists in the photometric surface brightness and the kinematic velocity field (both roughly 5 degrees, but in opposite directions) already hint at such a departure from our assumptions. (Statler & Smecker-Hane 1999) suggest that NGC 3379 might be triaxial. The system might also not have adequately relaxed. Indeed, the asymmetry of the velocity dispersion profile beyond $20''$ seems to corroborate the latter possibility, despite the lack of photometric evidence.

A more worrisome development, from a recent paper Sambhus et al. (2005), is the discovery

of two populations of PNe in NGC 4697, one younger and inherently brighter than the other, creating a bias in the measurements of the PN kinematics. Given its somewhat odd velocity field, it is entirely possible that NGC 3379 contains a bimodal population of PNe. A sample size of 50 PNe, however, is clearly unable to address these questions usefully. A larger sample of ellipticals combined with deeper observations are needed to investigate the relevant statistics.

10. Conclusions

We have reported on a search for PNe around four early-type galaxies using the RFP. We obtained reasonably sized samples in the case of the two Leo galaxies, NGC 3379 and NGC 3384, with adequate photometry and well determined radial velocities. The main limiting factor in our observations was the seeing; our data are read noise limited and better seeing would have improved the limiting magnitude of our survey. In our analysis of the RFP data cubes two realizations were essential in optimizing the size of the extracted PN samples. The power of our detections comes from using the data cube as a whole, as opposed to looking for point sources in each monochromatic RFP image. Secondly, applying the proper statistic is essential, along with a proper characterization of the reference distribution. A simple estimator yields mass-to-light ratios $\Upsilon_B \sim 10$ for the Leo galaxies, although a more sophisticated analysis for NGC 3379 gives an estimate that is a factor two lower, making it consistent with stellar population mass-to-light ratios. Although our models are relatively simple, they do produce conservative estimates of the mass-to-light ratios, and hence we do not find evidence for a dominant DM component inside a few R_e , confirming the recent work by Romanowsky et al. (2003).

In order to address questions about the existence of multimodal PN populations or the properties of PN kinematics as a function of host galaxy luminosity, we clearly need a larger and deeper set of surveyed galaxies. The RFP has been decommissioned, but successor instruments will be coming online in the very near future. The Prime Focus Imaging Spectrograph on the Southern African Large Telescope (11 m) will have Fabry-Perot image spectroscopy as one of its modes and will be ideally suited to extend current surveys of extragalactic PNe. It will be both competitive, considering depth and field of view, and complementary, being on the Southern hemisphere, to the Planetary Nebulae Spectrograph (Douglas et al. 2002).

Benoit Tremblay collaborated in some of the observations of this study. The staff at CTIO provided their usual excellent support for these observations. AS would like to acknowledge helpful conversations and email exchanges with E. Barnes, D. Chakrabarty, R. Méndez, R. Ciardullo, and J. Magorrian. This work was supported in part by the National Science Foundation through grants AST9731052 and AST0098650.

Facilities: Blanco (RFP), CTIO:1.5m

REFERENCES

Band, D., Ford, L., Matteson, J., Briggs, M., Paciesas, W., Pendleton, G., & Preece, R. 1997, ApJ, 485, 747

Binney, J., & Tremaine, S. 1987, Galactic Dynamics (Princeton, NJ: Princeton University Press)

Bridges, T., et al. 2003, Extragalactic Globular Clusters and their Host Galaxies, 25th meeting of the IAU, Joint Discussion 6, 17 July 2003, Sydney, Australia, 6,

Busarello, G., Capaccioli, M., D’Onofrio, M., Longo, G., Richter, G. & Zaggia, S. 1996, A&A, 314, 32

Capaccioli, M., Vietri, M., Held, E. V., & Lorenz, H. 1991, ApJ, 371, 535

Carollo, C. M., de Zeeuw, P. T., van der Marel, R. P., Danziger, I. J., & Qian, E. E., 1995, ApJ, 441, L25

Castro-Rodríguez, N., Aguerri, J. A. L., Arnaboldi, M., Gerhard, O., Freeman, K. C., Napolitano, N. R., & Capaccioli, M. 2003, A&A, 405, 803

Ciardullo, R., Feldmeier, J. J., Krelove, K., Jacoby, G. H., & Gronwal, C. 2002, ApJ, 566, 784

Ciardullo, R., Jacoby, G. H., & Dejonghe, H. B. 1993, ApJ, 414, 454

Ciardullo, R., Jacoby, G. H. & Ford, H. C. 1989, ApJ, 344, 715

Côté, P., McLaughlin, D. E., Cohen, J. G., & Blakeslee, J. P. 2003, ApJ, 591, 850

de Blok, W. J. G., Bosma, A., & McGaugh, S. 2003, MNRAS, 340, 657

de Vaucouleurs, G., & Capaccioli, M. 1979, ApJS, 40, 699

de Vaucouleurs, G., de Vaucouleurs, A., Corwin, H. G., Buta, R. J., Paturel, G., Fouque, P. 1991, Third Reference Catalog of Bright Galaxies, (New York: Springer-Verlag)

Diemand, J., Moore, B., & Stadel, J. 2004, MNRAS, 353, 624

Dopita, M. A., Jacoby, G. H., & Vassiliadis, E. 1992, ApJ, 389, 27

Douglas, N. G., et al. 2002, PASP, 114, 1234

Eadie, W. T., Drijard, D., James, F. E., Roos, M., & Sadoulet, B. 1971, Statistical Methods in Experimental Physics (New York: North-Holland)

Evans, N. W., Wilkinson, M. I., Perrett, K. M., & Bridges, T. J., 2003, ApJ, 583, 752

Ferguson, H. C., & Sandage, A. 1990, AJ, 100, 1

Ferrarese, L., et al. 2000, *ApJ*, 529, 745

Franx, M., Illingworth, G., & Heckman, T. 1989, *AJ*, 98, 538

Freeman, P. E., Graziani, C., Lamb, D. Q., Loredo, T. J., Fenimore, E. E., Murakami, T., & Yoshida, A. 1999, *ApJ*, 524, 753

Freeman, K. C., et al. 2000, in *ASP Conf. Ser.* 197, *Dynamics of Galaxies: from the Early Universe to the Present*, 15th IAP meeting held in Paris, France, July 9-13, 1999, ed. F. Combes, G. A. Mamon, and V. Charmandaris (San Francisco: ASP), 389

Gebhardt, K., et al. 1996, *AJ*, 112, 105

Gebhardt, K., et al. 2000, *AJ*, 119, 1157

Gerhard, O. E. 1993, *MNRAS*, 265, 213

Gerhard, O., Kronawitter, A., Saglia, R. P., & Bender, R. 2001, *AJ*, 121, 1936

Goudfrooij, P., Hansen, L., Jørgensen, H. E., Nørgaard-Nielsen, H. U., de Jong, T., & van den Hoek, L. B. 1994, *A&AS*, 104, 179

Hamuy, M., Walker, A. R., Suntzeff, N. B., Gigoux, P., Heathcote, S. R., & Phillips, M. M. 1992, *PASP*, 104, 533

Harris, W. E. 1990, *PASP*, 102, 949

Hernquist, L. 1990, *ApJ*, 356, 359

Hoaglin, D. C., Mosteller, F., & Tukey, J. W. 1983, *Wiley Series in Probability and Mathematical Statistics*, New York: Wiley, 1983, edited by Hoaglin, David C.; Mosteller, Frederick; Tukey, John W.

Hu, E. M., Cowie, L. L., & McMahon, R. G. 1998, *ApJ*, 502, L99

Hui, X., Ford, H. C., Freeman, K. C., & Dopita, M. 1995, *ApJ*, 449, 592

Keeton, C. R., 2001, *ApJ*, 561, 46

Kronawitter, A., Saglia, R. P., Gerhard, O., & Bender, R. 2000, *A&AS*, 144, 53

Kudritzki, R.-P., et al. 2000, *ApJ*, 536, 19

Loewenstein, M., & White, R. E., III 1999, *ApJ*, 518, 50

Longo, G., Zaggia, S. R., Busarello, G., & Richter, G. 1994, *A&AS*, 105, 433

Magorrian, J., & Ballantyne, D. 2001, *MNRAS*, 322, 702

Malin, D. F. 1984, in IAU Coll. 58, *Astronomy with Schmidt Type Telescopes*, ed. M. Capaccioli (Dordrecht: Reidel), 73

Malin, D. F., & Carter, D. 1983, *ApJ*, 274, 534

Mathews, W. G. & Brighenti, F., 2003, *ARA&A*, 41, 191

Mattox, J., et al. 1996, *ApJ*, 461, 396

McElroy, D. B., 1995, *ApJS*, 100, 105

Méndez, R. H., Riffeser, A., Kudritzki, R.-P., Matthias, M., Freeman, K. C., Arnaboldi, M., Capaccioli, M., & Gerhard, O. E. 2001, *ApJ*, 563, 135

Merritt, D. 1993, *ApJ*, 413, 79

Merritt, D., & Saha, P. 1993, *ApJ*, 409, 75

Metropolis, N., Rosenbluth, A., Rosenbluth, M., Teller, A., & Teller, E., 1953, *J. Chem. Phys.*, 21, 1087

Monet, D., Bird A., Canzian, B., Dahn, C., Guetter, H., Harris, H., Henden, A., Levine, S., Luginbuhl, C., Monet, A. K. B., Rhodes, A., Riepe, B., Sell, S., Stone, R., Vrba, F., Walker, R. 1998, *The USNO-A2.0 Catalogue*, (Washington DC: U.S. Naval Observatory)

Navarro, J. F., Frenk, C. S., & White, S. D. M. 1997, *ApJ*, 490, 493

Naylor, T. 1998, *MNRAS*, 296, 339

Neal, R. M., 2003, *Annals of Statistics*, 31, 705

Nolthenius, R., & Ford, H. 1986, *ApJ*, 305, 600

Ouchi, M., et al. 2003, *ApJ*, 582, 60

Peletier, R. F., Davies, R. L., Illingworth, G. D., Davis, L. E., & Cawson, M. 1990, *AJ*, 100, 1091

Peng, E. W., Ford, H. C., & Freeman, K. C. 2004, *ApJ*, 602, 685

Peng, E. W., Ford, H. C., & Freeman, K. C. 2005, preprint (astro-ph/0412449)

Perlmutter, S., et al. 1999, *ApJ*, 517, 565

Phillips, J. P. 2002, *A&A*, 393, 1027

Pottasch, S. R. 1984, *Planetary Nebulae*, (Dordrecht: Reidel)

Protassov, R., van Dyk, D. A., Connors, A., Kashyap, V. L., & Siemiginowska, A. 2002, *ApJ*, 571, 545

Ravindranath, S., Ho, L. C., Peng, C. Y., Filippenko, A. V., & Sargent, W. L. 2001, AJ, 122, 653

Riess, A. G., et al. 1998, AJ, 116, 1009

Romanowsky, A. J., Douglas, N. G., Arnaboldi, M., Kuijken, K., Merrifield, M. R., Napolitano, N. R., Capaccioli, M., & Freeman, K. C. 2003, Sci., 301, 1696

Romanowsky, A. J. & Kochanek, C. S., 2001, ApJ, 553, 722

Sambhus, N., Gerhard, O., & Mendez, R. H. 2005, preprint (astro-ph/0510499)

Schneider, S. E., 1989, ApJ, 343, 94

Schneider, S. E. et al., 1989, AJ, 97, 666

Secker, J. 1995, PASP, 107, 496

Sellwood, J. A. & Kosowsky, A., 2001, in: ASP Conf. Ser. 240: Gas and Galaxy Evolution, 311

Sluis, A. P. N., PhD. Thesis, Rutgers, NJ

Sofue, Y. & Rubin, V., 2001, ARA&A, 39, 137

Sparke, L. S., 2002, in: Proceedings of the Yale Cosmology Workshop "The Shapes of Galaxies and Their Dark Matter Halos", New Haven, Connecticut, USA, 28-30 May 2001, (Singapore: World Scientific), 178

Spergel, D. N., et al. 2003, ApJS, 148, 175

Statler, T. S., & Smecker-Hane, T. 1999, AJ, 117, 839

Stern, D., Bunker, A., Spinrad, H., & Dey, A. 2000, ApJ, 537, 73

Stetson, P. B. 1987, PASP, 99, 191

Stone, R. P. S. & Baldwin, J.A. 1983, MNRAS, 204, 347

Tonry, J.L., Dressler, A., Blakeslee, J. P., Ajhar, E. A., Fletcher, A. B., Luppino, G. A., Metzger, M. R., & Moore, C. B. 2001, ApJ, 546, 681

Tremblay, B. T., Merritt, D., & Williams T. B. 1995, ApJ, 443, L5

van de Hulst, H. C. & Reesinck, J. M. 1947, ApJ, 106, 121

van der Marel, R. P., & Franx, M. 1993, ApJ, 407, 525

Verde, L. et al., 2003, ApJS, 148, 195

Wilson, G., Kaiser, N., Luppino, G. A., & Cowie, L. L., 2001, ApJ, 555, 572

Table 1. The instrumental and detector setup.

	1994 April 7–10	1995 February 2–6
CCD	Tek 1k (CTIO #1, VEB)	Tek 1k (CTIO #2, Arcon)
Gain	$1.73 e^- \text{ ADU}^{-1}$	$1.25 e^- \text{ ADU}^{-1}$
Read noise	$3.22 e^-$	$4.33 e^-$
Image scale	$0.^{\prime\prime}70 \text{ pix}^{-1}$	$0.^{\prime\prime}35 \text{ pix}^{-1}$
Voigt FWHM	2.0 \AA	2.1 \AA
—Gaussian width $\Delta\lambda_G$	0.41 \AA	0.22 \AA
—Lorentzian width $\Delta\lambda_L$	0.89 \AA	1.0 \AA
Free spectral range $\Delta\lambda_{\text{FSR}}$	48 \AA	48 \AA
Filters (at CTIO)	5007-44, 5037-44	5007-44, 5037-44
Switching wavelength λ_s	5019 \AA	5022 \AA

Table 2. The observed fields.

field	α_c (hms)	δ_c ($^{\circ}$ '')	offset ($''$)	$N_{\text{obs}}^{\text{a}}$	$\Delta\lambda$ (Å)	$\langle\delta\lambda\rangle^{\text{b}}$ (Å)	N_{stars}	seeing ^c ($''$)	m_{lim}
NGC 1549	04 15 45	-55 35 27	6	28 (5)	5016–5043	1.0	3	1.5*	26.3
NGC 3379 E	10 47 54	+12 35 27	69	29 (2)	5011–5039	1.0	3	1.6*	26.1
NGC 3379 W	10 47 45	+12 34 25	77	33 (2)	5011–5040	1.0	3	1.5*	26.1
NGC 3384 C	10 48 17	+12 37 42	4	27 (2)	5012–5035	0.6	5	1.8	26.2
NGC 3384 N	10 48 17	+12 38 14	31	19 (1)	5012–5035	1.2	5	1.7	26.1
NGC 3384 W	10 48 12	+12 37 47	75	19 (1)	5012–5035	1.2	4	2.0	26.2
NGC 3384 E	10 48 26	+12 39 34	171	19 (1)	5010–5028	1.0	6	1.6	25.9
NGC 4636	12 42 50	+02 41 15	4	34 (4)	5013–5034	0.6	3	2.2*	26.7

Note. — NGC 1549, NGC 3379 and NGC 3384 E were observed during the 1995 run, the other fields during the 1994 run. For the 1994 (1995) run we took dome flats at 21 (28) RFP settings, spaced 1.25 Å (1.0 Å) apart, in sets of three images with an exposure time of 120 s (300 s) which were averaged to produce the final flatfield image.

^aThe number of images in the RFP stack with the number of observing nights in parentheses.

^bThe average wavelength separation of images in the RFP stack.

^cAn asterisk indicates that some of the data were taken under non-photometric conditions.

Table 3. Basic properties of the sample galaxies.

	NGC 1549	NGC 3379	NGC 3384	NGC 4636
Right ascension (2000.0; hms) ^a	04 15 44.00	10 47 49.60	10 48 16.90	12 42 49.87
Declination (2000.0; ° ' '') ^a	-55 35 30.0	12 34 53.9	12 37 45.5	02 41 16.0
Type ^b	E/S0 ₁	E1	SB(s)0-	E/S0 ₁
Radial velocity (km s ⁻¹) ^a	1220	911	704	938
Distance (Mpc) ^c	19.7	11.1	11.4	15.0
Total <i>B</i> magnitude ^a	10.72	10.24	10.85	10.34
<i>M_{B_T}</i> ^a	-20.75	-19.99	-19.43	-20.54
<i>R_e</i> (") ^b	91	35	50	177

^aFrom the NASA/IPAC Extragalactic DataBase (NED).

^bGalaxy classifications from RC3 (de Vaucouleurs et al. 1991).

^cUsing the mean distance modulus from Ferrarese et al. (2000), apart from NGC 1549 (Tonry et al. 2001).

Table 4. NGC 1549 and NGC 4636 Planetary Nebulae

ID	α	δ	λ_c	v_{helio}	σ_v	F_{pn}	m_{5007}	σ_m	S	Q
(1)	(2)	(3)	(4)	(5)	(6)	(7)	(8)	(9)	(10)	(11)
NGC 1549										
N1-1	4:15:35.96	-55:35:18.3	5026.2	1147	14	1.04	26.21	0.23	23.1	5.0
N1-2	4:15:42.65	-55:34:43.5	5032.9	1547	17	0.84	26.45	0.23	22.8	5.7
N1-3	4:15:44.86	-55:36:10.7	5033.8	1603	18	0.98	26.28	0.25	19.6	5.6
N1-4	4:15:48.31	-55:36:01.9	5024.7	1060	14	1.20	26.07	0.22	26.7	5.8
N1-5	4:15:51.14	-55:34:34.8	5025.1	1080	15	0.93	26.34	0.20	31.9	6.4
N1-6	4:15:51.75	-55:35:23.0	5027.6	1234	12	1.23	26.03	0.19	34.1	7.5
NGC 4636										
N4-1	12:42:51.53	2:40:49.9	5019.3	739	19	0.77	26.54	0.26	17.4	4.8
N4-2	12:42:52.09	2:40:24.9	5025.1	1086	21	0.75	26.58	0.23	23.3	7.1

Note. — Col. (1) N1 and N4 denote PNe found in NGC 1549 and NGC 4636, respectively; col. (2)–(3) right ascension (hms) and declination ($^{\circ}''$), where the uncertainty in each coordinate is $0.^{\circ}7$ (includes random and systematic uncertainty); col. (4) peak wavelength (\AA); col. (5) heliocentric line-of-sight velocity (km s^{-1}); col. (6) uncertainty in v_{helio} ; col. (7) emission line flux ($10^{-16} \text{ erg cm}^{-2} \text{ s}^{-1}$); col. (8) emission line magnitude $m_{5007} \equiv -2.5 \log(F) + 13.74$ (no extinction correction was made); col. (9) uncertainty in m_{5007} ; col. (10) test statistic S_{LR} ; col. (11) signal-to-noise ratio.

Table 5. NGC 3379 Planetary Nebulae

ID	α	δ	λ_c	v_{helio}	σ_v	F_{pn}	m_{5007}	σ_m	S	Q	ID_{cjf}	m_{cjf}	v_{cjf}
(1)	(2)	(3)	(4)	(5)	(6)	(7)	(8)	(9)	(10)	(11)	(12)	(13)	(14)
E01	10:47:48.73	12:35:24.8	5024.8	1083	13	1.68	25.69	0.21	27.5	6.0
E02	10:47:49.17	12:35:42.4	5017.6	653	17	1.61	25.74	0.23	26.3	5.5
E03	10:47:49.47	12:35:35.3	5023.6	1009	17	1.52	25.80	0.19	32.6	7.0	9	25.66	...
E04	10:47:49.66	12:36:02.5	5021.0	853	18	1.11	26.14	0.23	23.4	5.8
E05	10:47:49.94	12:35:40.2	5018.3	694	13	1.97	25.52	0.22	26.3	6.1	20	25.84	...
E06	10:47:50.30	12:35:13.0	5025.0	1098	12	2.03	25.49	0.18	37.1	6.7
E07	10:47:51.06	12:35:01.5	5023.0	974	17	1.78	25.64	0.22	25.4	6.9	12	25.76	...
E08	10:47:51.15	12:35:15.4	5018.8	723	19	1.85	25.59	0.26	18.8	4.8	36	26.10	...
E09	10:47:51.26	12:34:51.2	5025.8	1141	17	1.73	25.66	0.21	26.4	6.3
E10	10:47:51.40	12:35:31.5	5023.8	1022	13	2.26	25.37	0.15	54.7	9.0	2	25.33	1061
E11	10:47:51.59	12:35:43.3	5025.4	1116	13	1.73	25.66	0.15	53.4	8.2	6	25.53	...
E12	10:47:51.68	12:34:47.3	5023.6	1013	10	2.44	25.29	0.17	39.3	6.9	23	25.92	...
E13	10:47:52.03	12:35:11.0	5018.0	675	20	1.76	25.64	0.22	25.3	4.7
E14	10:47:52.11	12:34:43.5	5022.4	942	13	2.19	25.41	0.15	50.3	9.1	1	25.28	936
E15	10:47:52.28	12:35:40.1	5023.3	991	13	1.81	25.62	0.17	45.1	8.0	14	25.77	...
E16	10:47:52.33	12:36:05.7	5020.8	844	11	1.75	25.65	0.18	35.6	6.7	16	25.78	832
E17	10:47:53.34	12:36:17.2	5021.4	881	14	1.25	26.02	0.22	23.5	6.0
E18	10:47:54.83	12:36:24.8	5020.8	843	13	1.47	25.84	0.20	31.0	5.6	30	26.00	...
E19	10:47:55.12	12:36:17.1	5021.3	873	13	1.43	25.87	0.20	28.8	6.7	60	26.37	...
E20	10:47:55.43	12:34:51.5	5023.5	1007	17	1.28	25.99	0.22	24.2	6.0	38	26.14	1021
E21	10:47:55.50	12:34:46.0	5020.9	850	13	1.57	25.77	0.21	28.3	6.6
E22	10:47:55.76	12:35:40.5	5020.2	806	19	1.43	25.87	0.27	17.0	4.9
E23	10:47:56.07	12:35:42.0	5015.2	510	17	1.46	25.85	0.22	23.8	5.4
E24	10:47:56.86	12:36:14.5	5019.2	748	21	1.16	26.10	0.27	17.0	4.3	28	25.98	...
E25	10:47:56.90	12:34:20.7	5015.4	521	17	1.30	25.97	0.27	15.8	4.6
E26	10:47:56.92	12:35:31.2	5021.9	910	14	1.36	25.93	0.20	28.5	6.2	39	26.15	...
E27	10:47:58.10	12:34:42.2	5011.6	291	23	1.71	25.68	0.30	22.1	5.4
E28	10:47:59.21	12:35:10.6	5018.7	719	13	1.79	25.63	0.20	29.8	6.8	10	25.68	...
W01	10:47:41.41	12:35:12.0	5020.0	797	17	1.09	26.17	0.22	23.9	3.6
W02	10:47:41.67	12:34:05.5	5018.7	720	17	1.15	26.11	0.23	22.7	5.5
W03	10:47:41.71	12:34:32.2	5023.4	1004	15	1.32	25.96	0.20	28.4	6.9	48	26.26	...
W04	10:47:42.55	12:35:31.7	5015.3	517	17	1.12	26.14	0.25	18.6	4.3
W05	10:47:42.56	12:35:08.9	5023.8	1025	13	1.39	25.91	0.15	52.0	8.9	41	26.18	...
W06	10:47:42.92	12:35:09.6	5022.0	919	15	1.25	26.02	0.21	28.1	6.8	62	26.40	...
W07	10:47:44.73	12:35:07.6	5024.0	1039	12	1.17	26.09	0.19	34.7	7.4
W08	10:47:45.21	12:34:59.7	5023.1	982	12	1.48	25.83	0.17	39.5	7.2	29	25.99	977

Table 5—Continued

ID	α	δ	λ_c	v_{helio}	σ_v	F_{pn}	m_{5007}	σ_m	S	Q	ID _{cjf}	m_{cjf}	v_{cjf}
(1)	(2)	(3)	(4)	(5)	(6)	(7)	(8)	(9)	(10)	(11)	(12)	(13)	(14)
W09	10:47:45.26	12:35:17.3	5018.7	720	11	1.50	25.82	0.16	48.2	8.6	19	25.83	716
W10	10:47:45.39	12:33:37.9	5018.2	691	18	1.24	26.03	0.23	25.0	4.7	50	26.28	726
W11	10:47:45.67	12:34:13.4	5017.4	640	18	1.36	25.93	0.23	25.2	4.9	63	26.40	...
W12	10:47:45.83	12:35:06.7	5025.7	1138	15	1.06	26.19	0.21	27.6	7.3
W13	10:47:46.23	12:33:37.5	5026.9	1212	16	1.02	26.24	0.24	20.4	5.5	40	26.15	...
W14	10:47:46.24	12:34:10.5	5024.7	1078	15	1.08	26.18	0.22	25.0	5.7	59	26.37	...
W15	10:47:46.72	12:33:18.7	5015.6	531	20	1.16	26.10	0.26	17.9	4.3
W16	10:47:46.94	12:34:06.0	5024.2	1050	16	1.01	26.25	0.22	24.0	4.4
W17	10:47:47.25	12:35:01.3	5028.6	1310	11	1.53	25.80	0.18	36.2	6.9	11	25.75	...
W18	10:47:47.29	12:34:47.1	5026.2	1168	12	1.48	25.83	0.18	37.6	7.4
W19	10:47:48.10	12:35:00.1	5020.0	797	13	1.54	25.79	0.23	22.2	5.9
W20	10:47:48.34	12:34:38.0	5024.3	1053	13	1.91	25.56	0.15	54.0	9.8	7	25.63	1060
W21	10:47:48.58	12:33:32.9	5019.3	757	18	1.37	25.92	0.21	27.0	5.5	49	26.28	...
W22	10:47:48.65	12:35:03.5	5022.3	932	10	2.40	25.31	0.14	61.5	9.4
W23	10:47:48.85	12:34:41.6	5020.2	807	17	1.58	25.76	0.25	21.4	4.5
W24	10:47:48.94	12:33:40.3	5023.4	1001	14	1.22	26.04	0.19	33.4	6.3	27	25.96	985
W25	10:47:48.97	12:34:27.6	5019.4	758	15	1.67	25.70	0.18	39.0	7.3	42	26.20	...
W26	10:47:49.97	12:34:38.8	5021.0	858	16	1.95	25.54	0.21	30.6	5.9

Note. — Col. (1) E and W denote PNe found in the East and West fields, respectively; col. (2)–(3) right ascension (hms) and declination ($^{\circ}''$), where the uncertainty in each coordinate is $0.^{\circ}4$ (includes random and systematic uncertainty); col. (4) peak wavelength (\AA); col. (5) heliocentric line-of-sight velocity (km s^{-1}); (6) uncertainty in v_{helio} ; col. (7) emission line flux ($10^{-16} \text{ erg cm}^{-2} \text{ s}^{-1}$); col. (8) emission line magnitude $m_{5007} \equiv -2.5 \log(F) + 13.74$ (no extinction correction was made); col. (9) uncertainty in m_{5007} ; col. (10) test statistic S_{LR} ; col. (11) signal-to-noise ratio; col. (12)–(13) corresponding ID and m_{5007} from Ciardullo et al. (1989); col. (14) corresponding line-of-sight velocity from Ciardullo et al. (1993).

Table 6. NGC 3384 Planetary Nebulae

ID	α	δ	λ_c	v_{helio}	σ_v	F_{pn}	m_{5007}	σ_m	S	^a	Q	ID _{cjf}	m_{cjf}
(1)	(2)	(3)	(4)	(5)	(6)	(7)	(8)	(9)	(10)	(11)	(12)	(12)	(13)
E01	10:48:21.63	12:38:43.9	5015.2	497	14	1.32	25.96	0.21	27.5 (19)	5.8	49	26.38	
E02	10:48:24.42	12:38:43.6	5016.5	576	11	1.55	25.78	0.18	38.0 (19)	6.8	1	25.59	
E03	10:48:25.18	12:39:36.2	5016.3	564	13	1.07	26.19	0.23	23.4 (19)	6.4	11	25.93	
W01	10:48:09.00	12:37:44.6	5020.8	812	13	1.10	26.16	0.24	21.4 (19)	6.7	21	26.05	
W02	10:48:09.63	12:37:36.7	5021.2	838	8	1.79	25.63	0.16	48.9 (18)	9.8	10	25.90	
W03	10:48:10.43	12:36:54.5	5021.3	844	12	1.31	25.97	0.21	26.8 (19)	8.2	56	26.43	
W04	10:48:11.56	12:37:32.9	5020.6	800	10	1.35	25.93	0.14	61.5 (45)	12.4	7	25.81	
W05	10:48:11.85	12:37:21.2	5021.5	857	5	2.58	25.23	0.08	172.6 (44)	17.1	6	25.73	
W06	10:48:11.97	12:36:27.4	5022.0	886	8	1.90	25.56	0.16	48.6 (18)	9.5	8	25.85	
W07	10:48:12.29	12:36:53.1	5021.2	838	17	0.90	26.37	0.20	28.8 (35)	8.4	68	26.58	
W08	10:48:12.80	12:36:53.8	5022.2	896	8	1.92	25.55	0.11	107.0 (42)	16.6	2	25.63	
W09	10:48:13.25	12:38:02.3	5022.6	920	12	0.80	26.51	0.17	39.4 (61)	9.6	46	26.36	
W10	10:48:13.28	12:37:52.1	5020.6	800	9	0.95	26.32	0.16	45.8 (62)	9.6	43	26.34	
W11	10:48:13.41	12:38:06.9	5018.9	698	13	0.92	26.36	0.18	37.2 (61)	8.7	12	25.94	
W12	10:48:13.49	12:37:10.5	5021.0	826	11	1.29	25.99	0.15	59.9 (51)	10.9	28	26.11	
W13	10:48:13.51	12:37:02.8	5022.6	923	14	0.86	26.42	0.23	24.3 (44)	7.2	14	25.96	
W14	10:48:13.64	12:36:46.1	5021.9	883	7	1.88	25.57	0.10	112.8 (42)	15.0	9	25.86	
W15	10:48:14.17	12:36:39.0	5019.8	754	17	0.86	26.43	0.21	26.4 (45)	6.9	
W16	10:48:14.25	12:37:04.6	5020.6	800	11	1.01	26.25	0.17	39.5 (63)	8.9	59	26.45	
W17	10:48:14.37	12:36:47.7	5021.3	842	11	1.01	26.25	0.18	34.6 (44)	8.2	37	26.30	
W18	10:48:14.38	12:37:23.9	5021.0	826	11	1.07	26.19	0.16	45.3 (64)	10.5	
W19	10:48:14.60	12:36:59.9	5021.2	839	11	1.23	26.03	0.17	39.4 (47)	8.3	
W20	10:48:14.87	12:37:25.8	5021.4	847	9	1.65	25.71	0.11	93.2 (62)	13.5	3	25.66	
W21	10:48:15.12	12:38:08.3	5019.5	735	11	0.99	26.28	0.19	33.0 (62)	8.9	94	26.96	
W22	10:48:16.00	12:37:03.3	5020.3	781	14	0.78	26.54	0.22	22.9 (64)	7.1	
W23	10:48:16.03	12:38:02.9	5020.9	821	11	1.22	26.04	0.18	36.9 (61)	8.4	24	26.07	
W24	10:48:16.12	12:37:17.0	5023.2	956	9	1.16	26.10	0.16	46.3 (63)	10.9	34	26.20	
W25	10:48:16.17	12:37:09.2	5021.0	824	14	0.94	26.32	0.21	27.5 (61)	9.1	
W26	10:48:16.55	12:38:09.9	5019.8	752	17	0.93	26.34	0.20	28.4 (59)	8.1	33	26.18	
W27	10:48:16.81	12:37:20.1	5023.1	951	11	1.42	25.88	0.16	45.9 (59)	10.4	18	25.99	
W28	10:48:17.03	12:38:27.3	5019.6	741	11	1.38	25.91	0.16	44.8 (43)	9.9	4	25.67	
W29	10:48:17.52	12:37:10.5	5021.4	847	11	1.20	26.06	0.16	45.7 (44)	9.6	57	26.44	
W30	10:48:17.58	12:38:07.8	5018.8	696	15	1.17	26.09	0.23	23.3 (42)	7.0	5	25.71	
W31	10:48:17.91	12:38:09.3	5018.6	679	20	0.90	26.37	0.26	17.5 (46)	6.3	
W32	10:48:17.98	12:38:22.2	5017.2	599	14	1.04	26.22	0.21	28.8 (45)	7.9	
W33	10:48:18.07	12:38:44.0	5018.4	671	11	1.76	25.65	0.19	31.4 (25)	7.3	
W34	10:48:18.12	12:36:36.5	5019.4	729	14	1.36	25.93	0.21	27.2 (25)	7.2	22	26.06	

Table 6—Continued

ID	α	δ	λ_c	v_{helio}	σ_v	F_{pn}	m_{5007}	σ_m	S	^a	Q	ID _{cjf}	m_{cjf}
(1)	(2)	(3)	(4)	(5)	(6)	(7)	(8)	(9)	(10)	(11)	(12)	(13)	
W35	10:48:18.58	12:38:18.8	5018.5	676	10	1.51	25.81	0.17	42.0 (43)	9.1	16	25.98	
W36	10:48:18.83	12:37:15.4	5019.3	721	11	1.09	26.17	0.21	28.2 (41)	8.2	
W37	10:48:19.18	12:37:30.5	5018.4	672	18	0.85	26.43	0.25	19.8 (41)	6.9	50	26.38	
W38	10:48:19.40	12:38:16.4	5017.3	606	16	1.03	26.23	0.24	22.4 (44)	6.4	
W39	10:48:19.64	12:37:26.0	5019.7	747	16	1.10	26.15	0.23	26.0 (42)	6.6	
W40	10:48:19.73	12:36:44.5	5020.7	809	11	1.33	25.95	0.18	38.6 (27)	7.9	44	26.35	
W41	10:48:19.73	12:38:16.1	5016.9	583	10	1.26	26.01	0.18	38.5 (45)	8.8	40	26.31	
W42	10:48:20.41	12:38:03.5	5018.2	659	16	0.91	26.36	0.26	18.8 (44)	6.1	
W43	10:48:20.50	12:38:53.7	5018.0	643	13	1.52	25.81	0.23	21.8 (19)	6.5	20	26.04	
W44	10:48:20.75	12:38:21.7	5016.8	572	11	1.29	25.99	0.18	36.0 (45)	8.6	19	26.01	
W45	10:48:20.88	12:37:29.0	5020.0	766	8	1.42	25.88	0.14	62.3 (45)	10.8	83	26.73	
W46	10:48:20.92	12:38:05.7	5018.0	648	19	1.00	26.26	0.22	24.2 (44)	6.6	53	26.41	
W47	10:48:20.93	12:38:08.1	5017.4	607	12	1.03	26.23	0.23	23.3 (43)	6.8	

Note. — Col. (1) E and W denote PNe found in the East and West fields, respectively; col. (2)–(3) right ascension (hms) and declination ($^{\circ}''$), where the uncertainty in each coordinate is $0''.4$ (includes random and systematic uncertainty); col. (4) peak wavelength (\AA); col. (5) heliocentric line-of-sight velocity (km s^{-1}); col. (6) uncertainty in v_{helio} ; col. (7) emission line flux ($10^{-16} \text{ erg cm}^{-2} \text{ s}^{-1}$); col. (8) emission line magnitude $m_{5007} \equiv -2.5 \log(F) + 13.74$ (no extinction correction was made); col. (9) uncertainty in m_{5007} ; col. (10) test statistic S_{LR} (number of data points in spectrum); col. (11) signal-to-noise ratio; col. (12)–(13) corresponding ID and m_{5007} from Ciardullo et al. (1989).

^aThe spectra have a wide range in their number of data points and we determine $S_c(\alpha)$ for regions with one, two, or three pointing separately. Hence, the values of S listed in table 6 are not always directly comparable.

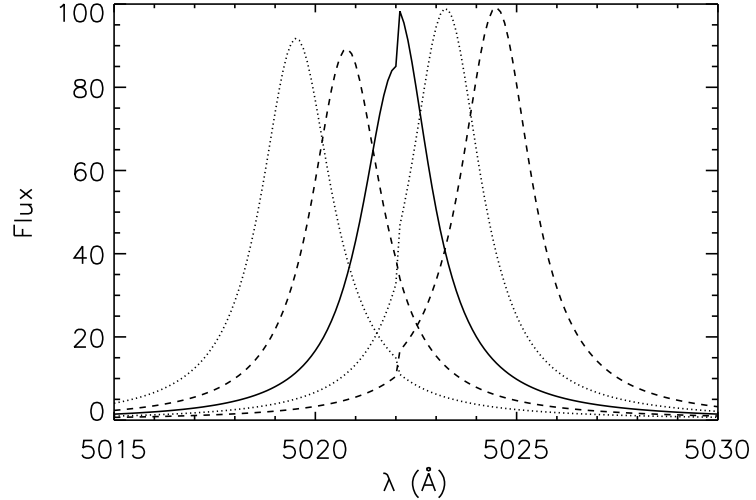


Fig. 1.— Line profiles of five PNe of equal brightness with wavelengths 1.25 Å apart. The solid line is a PN at a wavelength of 5022 Å, which is also the switching wavelength. The line profiles take into account the effects of filter switching (jump) and flatfielding (luminosity bias). The flux units are arbitrary. Different line styles were used for clarity.

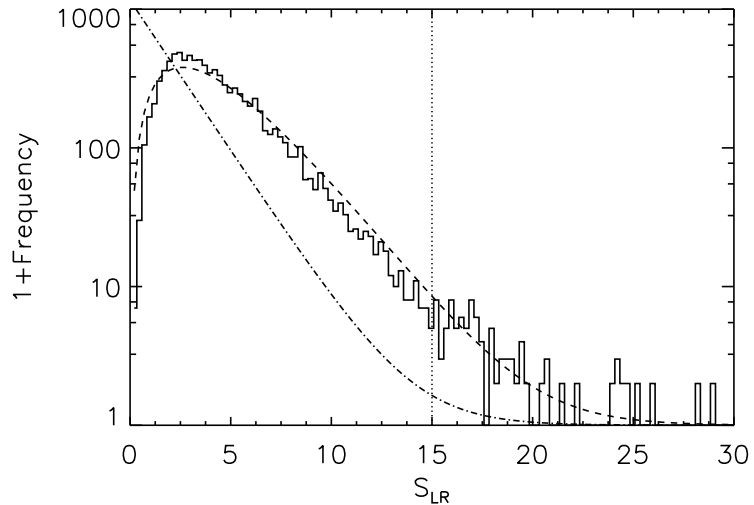


Fig. 2.— Histogram of the S_{LR} values from a simulated set of blank stacks based on the observations of the NGC 3379 East field. Note the logarithmic scale of the vertical axis. The vertical dotted line indicates the 1% upper tail of the distribution. The dot-dashed line is a χ^2 distribution, normalized to our sample size. The dashed line is a $\chi^2_{4.6}$ distribution, similarly normalized, plotted for comparison.

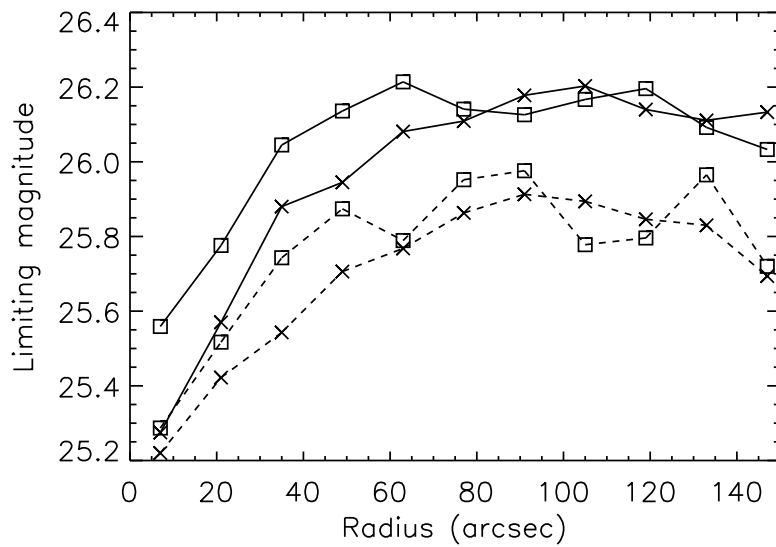


Fig. 3.— Limiting magnitude as a function of the distance to the center of NGC 3379. The crosses and squares represent the East and West field, respectively. The solid lines are the limiting magnitudes using the LR statistic; the dashed lines using the *F*-statistic.

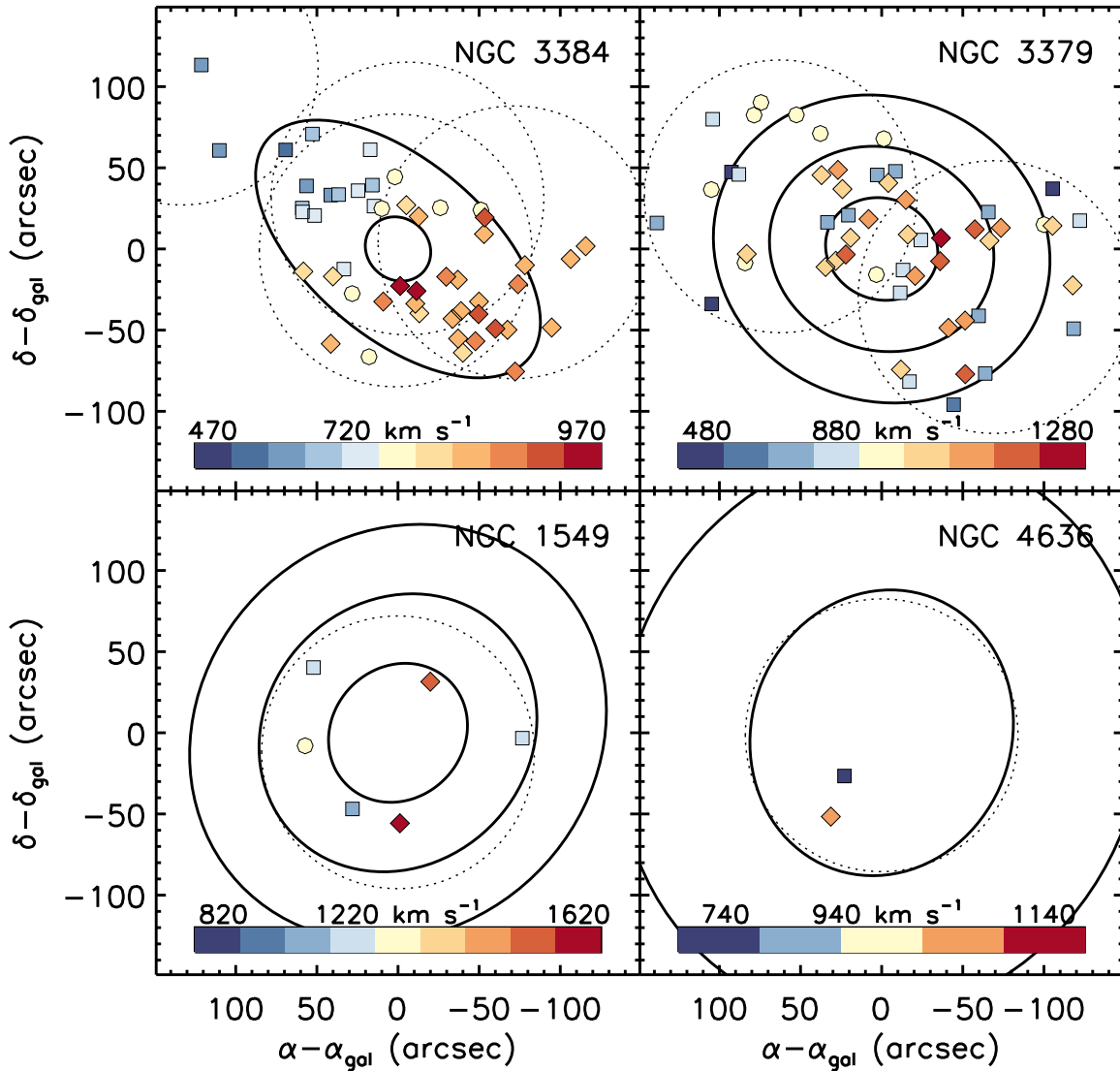


Fig. 4.— Line-of-sight velocities of the PNe in our galaxy sample. Dotted lines indicate the various pointings for each galaxy (see Table 2); solid lines are the isophotes at R_e , $2R_e$, and $3R_e$, except for NGC 3384 with isophotes at R_e (bulge) and $\mu_B = 25$ mag arcsec $^{-2}$ (disk). Red diamonds (blue squares) indicate PNe moving at radial velocities greater (less) than the systemic velocity; buff circles show radial velocities close to the systemic velocity. North is up and East is to the left.

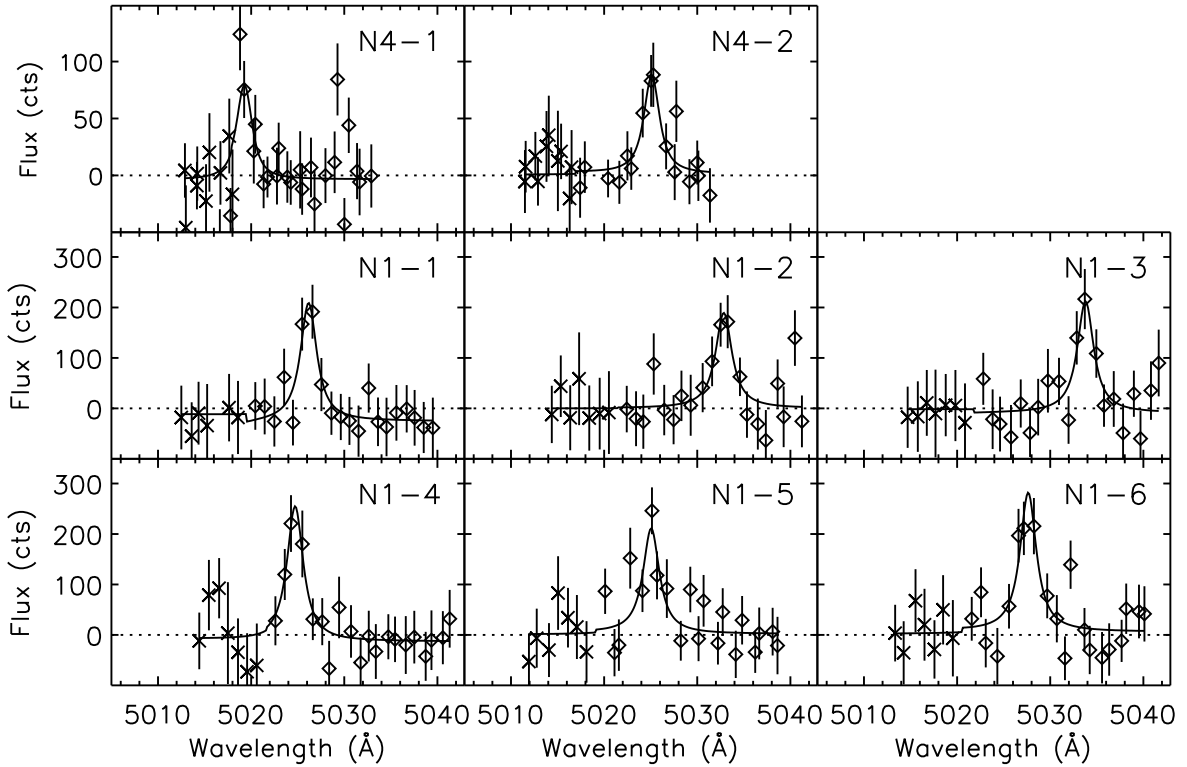


Fig. 5.— RFP spectra of the NGC 1549 and NGC 4636 PNe. Crosses denote observations under the 5007-44 filter, squares the 5037-44 filter. The curve is the best fit line profile as described by equation 2. The PN ID from Table 4 is shown in the top right corner of each spectrum. Note that the flux scales between the two sets of PNe are not directly comparable. Figures 5.1–5.7 are available in the electronic edition of the Journal. The printed edition contains only a sample.

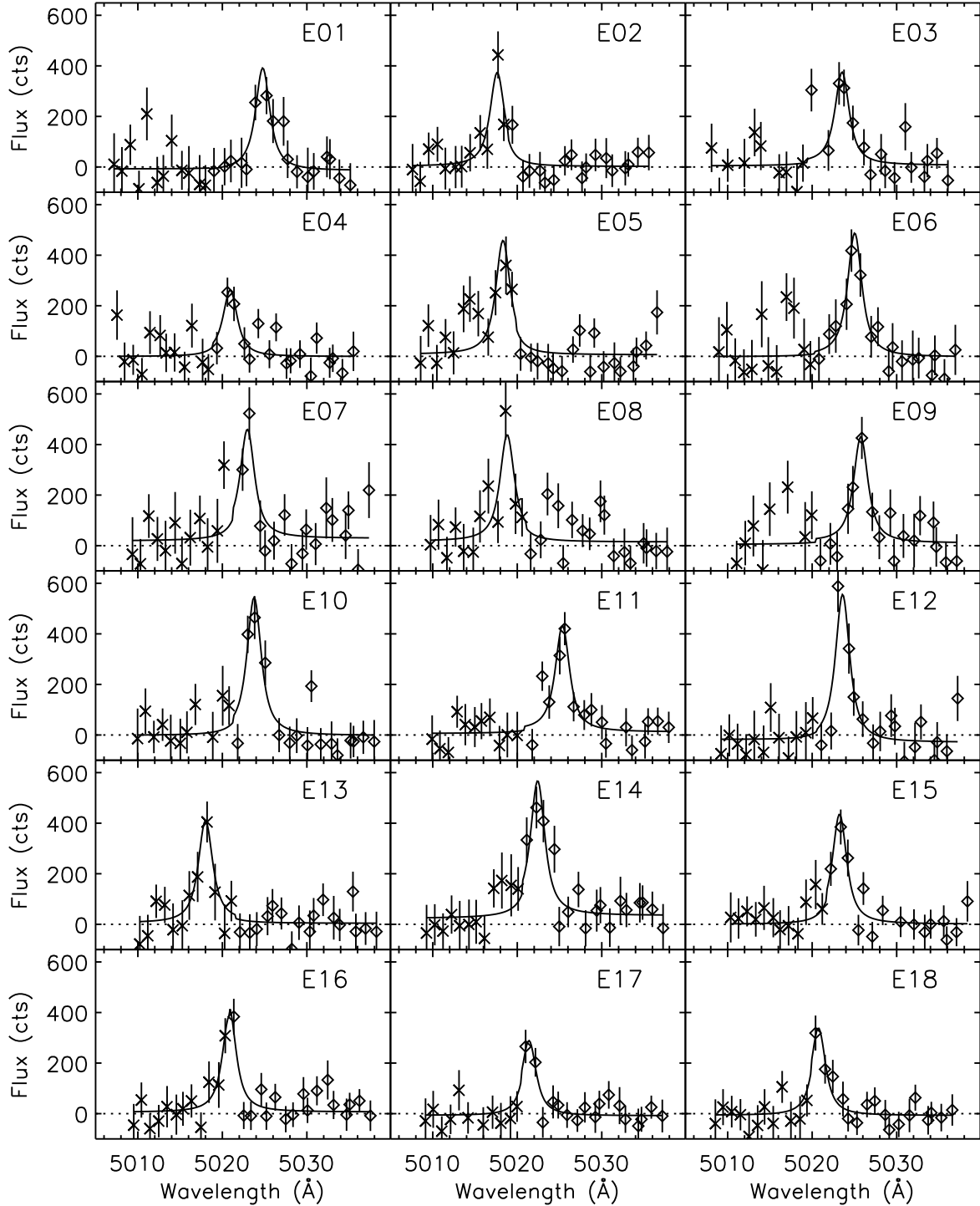


Fig. 5.2.— RFP spectra of the NGC 3379 PNe. Crosses denote observations under the 5007-44 filter, squares the 5037-44 filter. The curve is the best fit line profile as described by equation 2. The PN ID from Table 5 is shown in the top right corner of each spectrum. *Online only.*

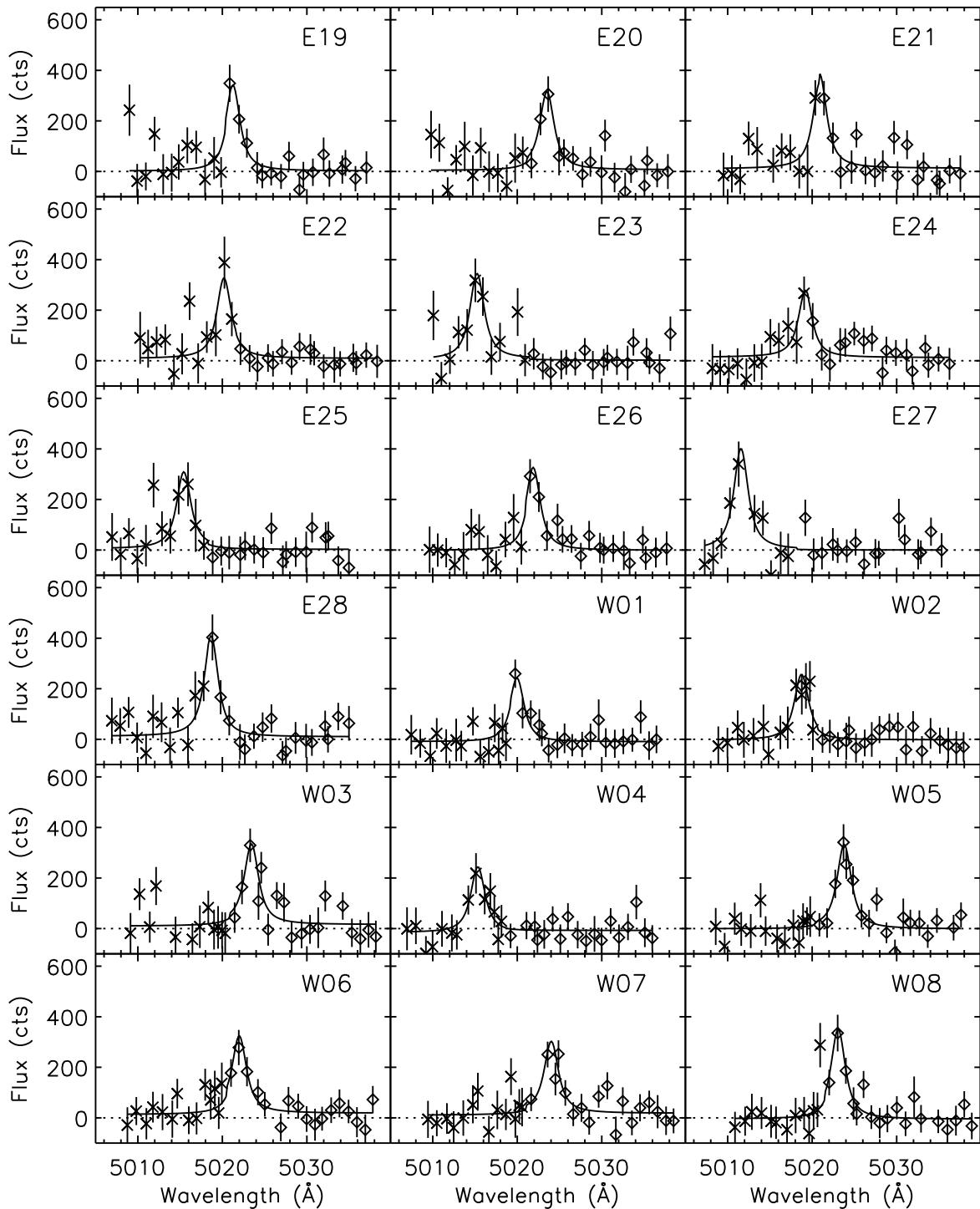


Fig. 5.3.— Continued from Fig. 5.2. *Online only.*

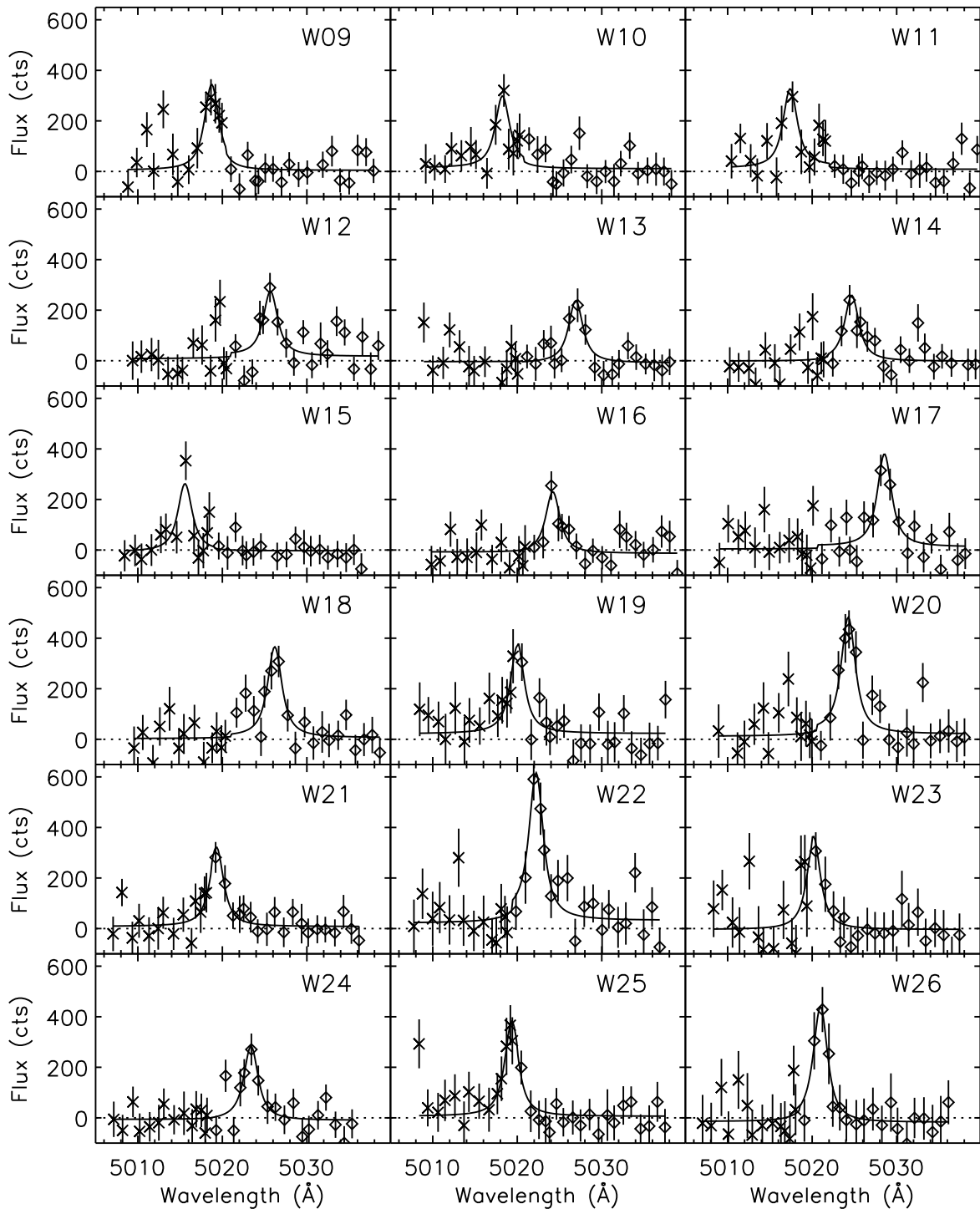


Fig. 5.4.— Continued from Fig. 5.3. *Online only.*

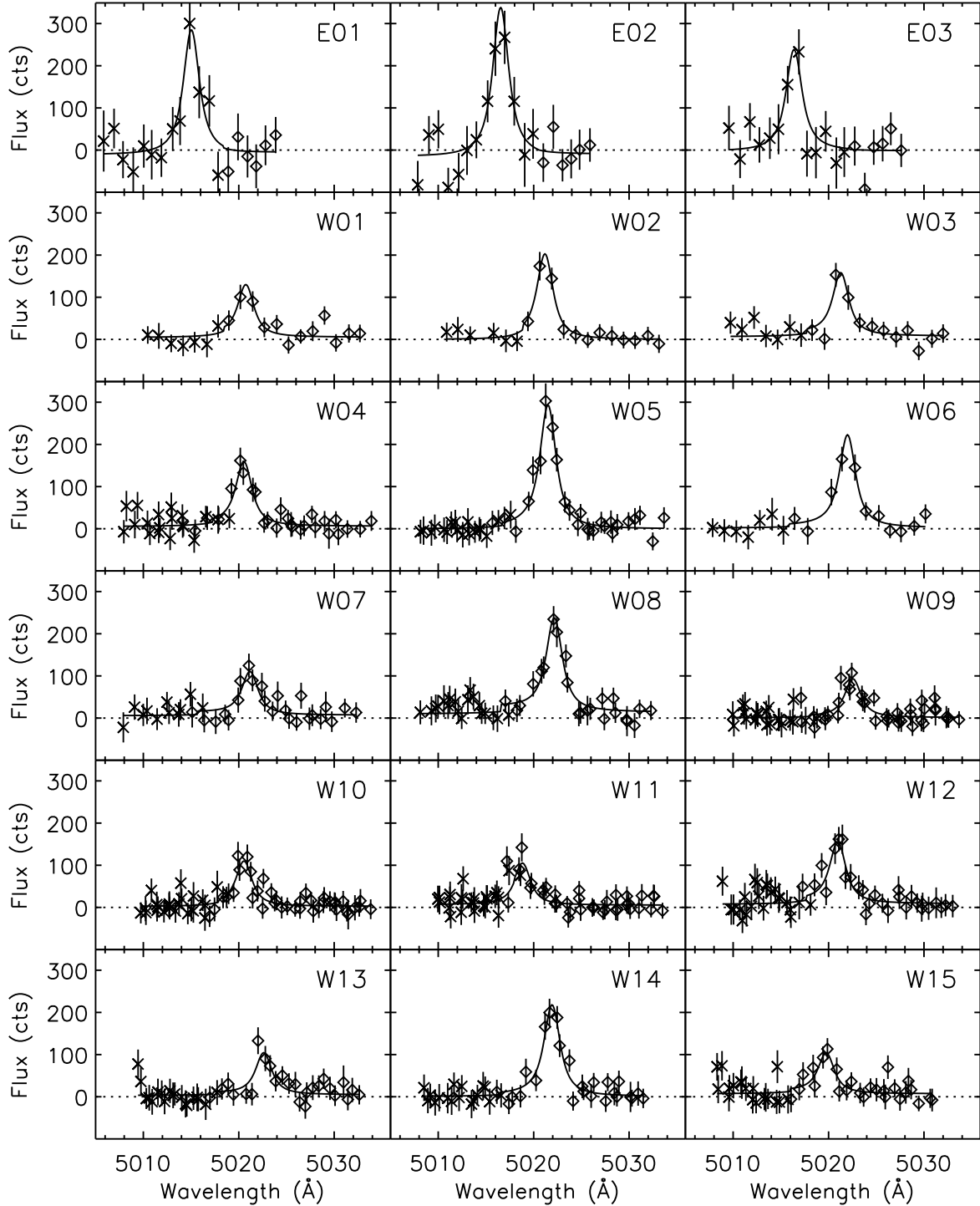


Fig. 5.5.— RFP spectra of the NGC 3384 PNe. Crosses denote observations under the 5007-44 filter, squares the 5037-44 filter. The curve is the best fit line profile as described by equation 2. The PN ID from Table 6 is shown in the top right corner of each spectrum. The PNe marked with E (W) were taken on the 1995 (1994) run and the flux scales are not directly comparable between the two runs. Note the changing ranges for the flux scales. *Online only.*

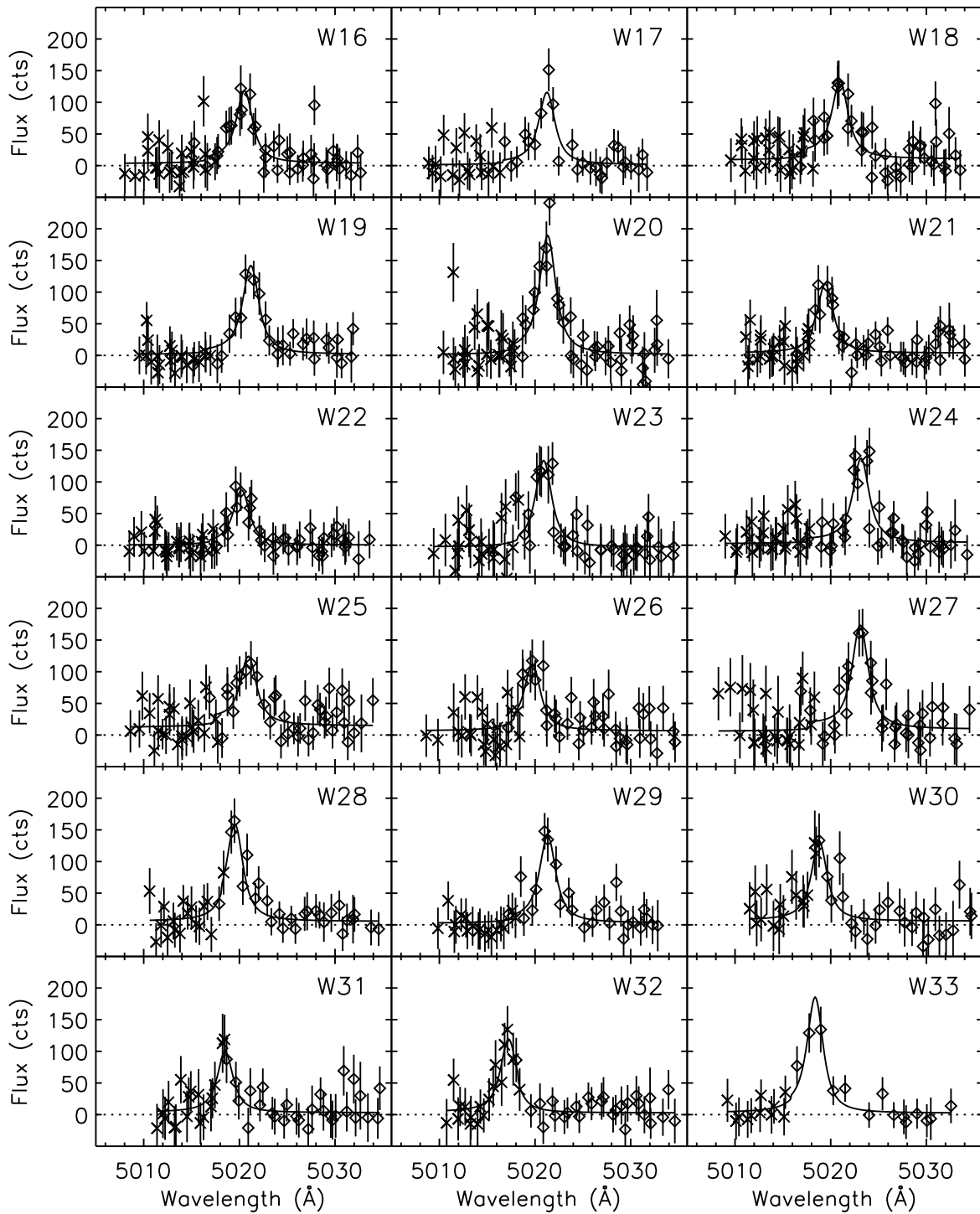


Fig. 5.6.— Continued from Fig. 5.5. *Online only.*

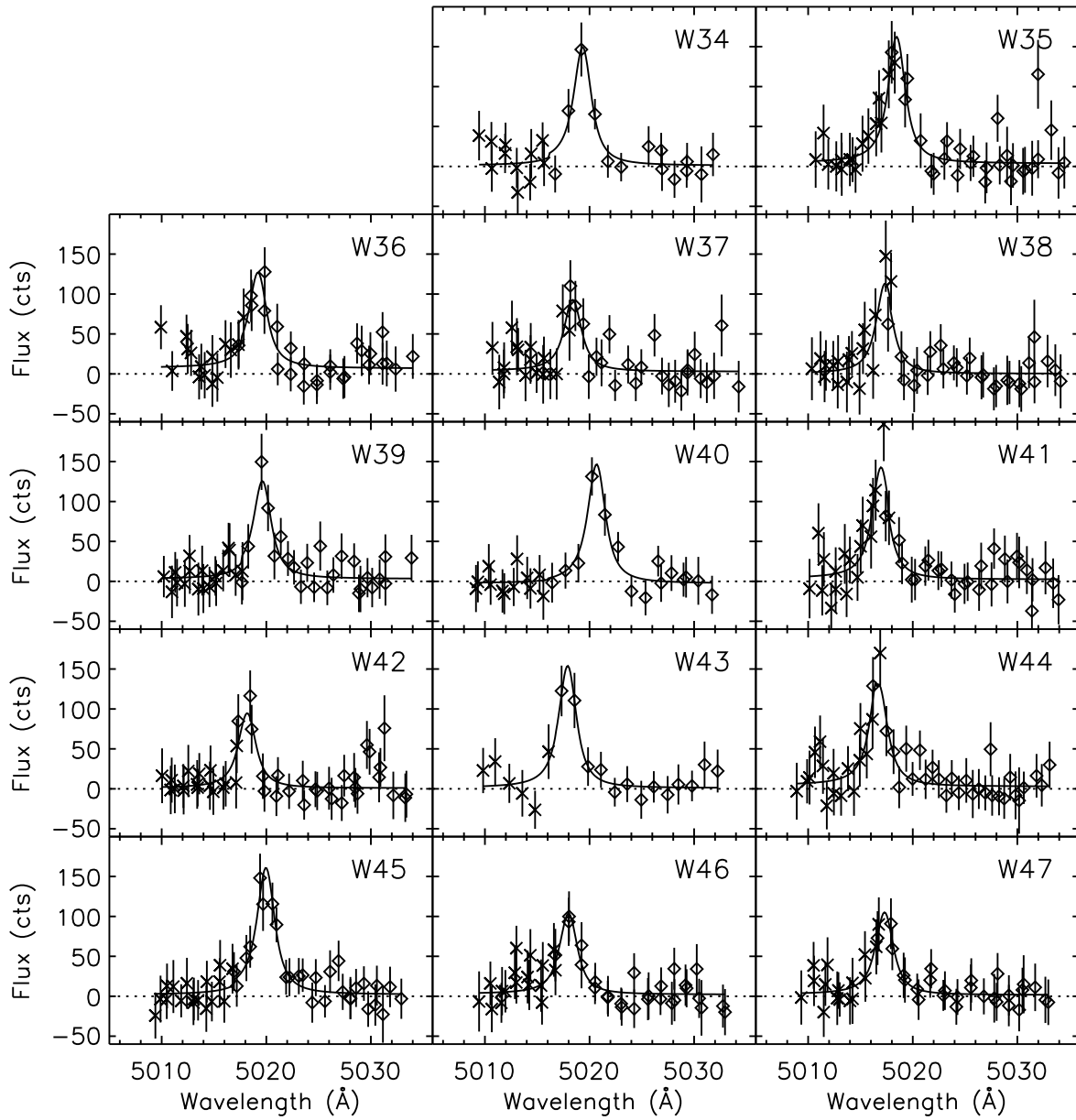


Fig. 5.7.— Continued from Fig. 5.6. *Online only.*

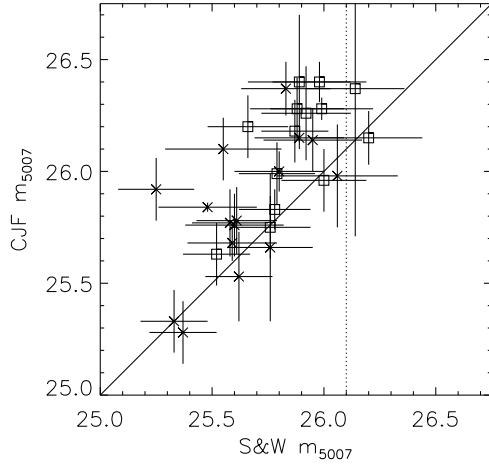


Fig. 6.— Comparison of the m_{5007} magnitudes of NGC 3379 in our sample (S&W) and those found by Ciardullo et al. (1989, CJF). Unspecified magnitude uncertainties in the latter sample were assumed to be 0.14 mag. PNe in the East and West field are indicated by squares and crosses, respectively. The solid line indicates exact correspondence between the two magnitude measurements; the dotted line the limiting magnitude of our survey.

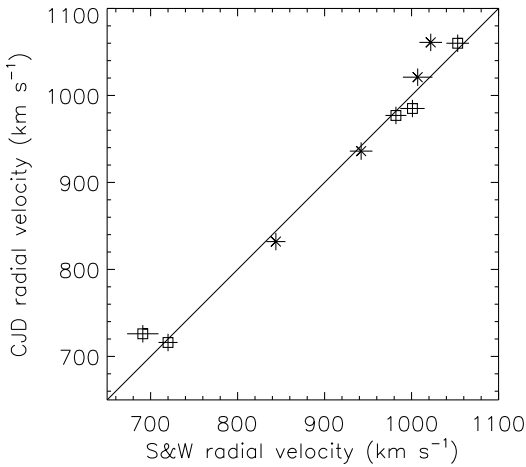


Fig. 7.— Comparison of the line-of-sight velocities of PNe in NGC 3379 determined by Ciardullo et al. (1993, CJD) and those of our sample (S&W). We assumed a velocity uncertainty of 10 km s^{-1} for the former. PNe in the East and West field are indicated by squares and crosses, respectively. The solid line indicates exact correspondence between the two velocity measurements.

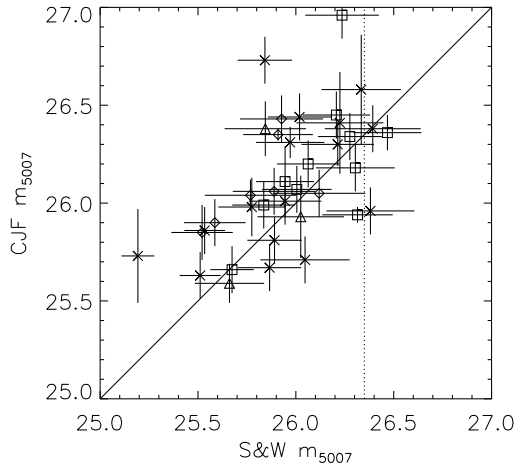


Fig. 8.— Comparison of the m_{5007} magnitudes of NGC 3384 in our sample (S&W) and those found by Ciardullo et al. (1989, CJF). Unspecified magnitude uncertainties in the latter sample were assumed to be 0.12 mag. The different symbols indicate the run and amount of data points in the spectra: triangles - 1995 run (East field); diamonds, crosses and squares - data from one, two or three pointings, respectively. The solid line indicates exact correspondence between the two magnitudes. The vertical dashed line is the average limiting magnitude of our sample, but note that the limiting magnitude for the 1995 run is 25.9.

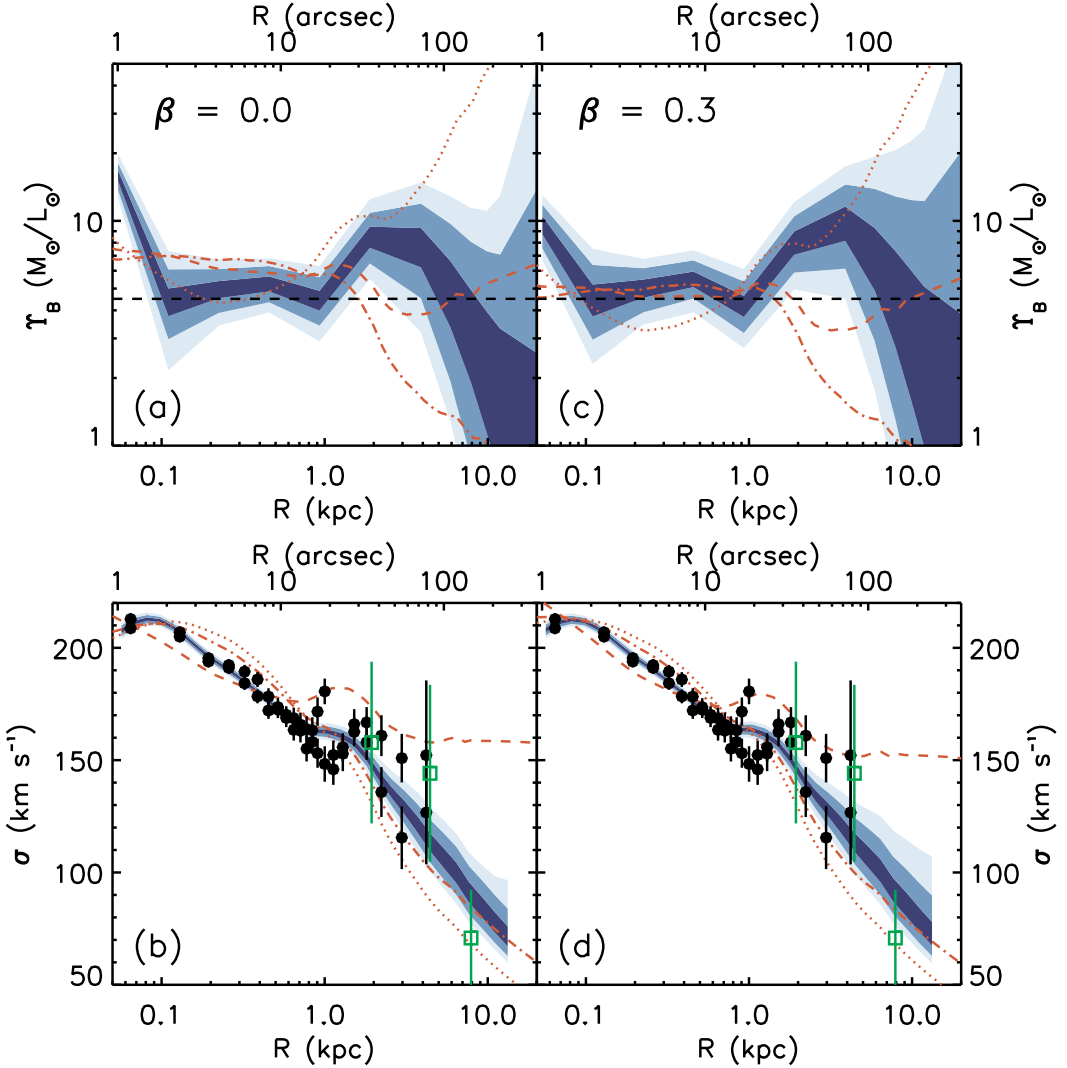


Fig. 9.— Results from two MCMC runs for NGC 3379, one assuming isotropy ($\beta = 0$, left column) and one assuming radial anisotropy ($\beta = 0.3$, right column). Credible regions (shades of blue) in each figure encompass, from the outside inwards, 99%, 90% and 50% of the posterior distribution. The red curves are the best fit results for a Hernquist model (dot-dashed), an NFW profile (dashed), and a pseudo-isothermal sphere (dotted). Figures (a) and (c): the local mass-to-light ratio $\Upsilon(r)$. The dashed line is the dynamical mass-to-light estimate from Gerhard et al. (2001). Figures (b) and (c): the agreement with the data, where the filled symbols are the data from Statler & Smecker-Hane (1999) (error bars of less than 2.5 km s^{-1} have been suppressed) and the green squares are the root-mean-square velocities of the PNe (this paper and Ciardullo et al. (1993)) in three bins with an equal number of PNe in each bin. The binning is only applied for clarity in the figure and plays no role in our actual dynamical analysis.